# Crustal contamination and hybridization of an embryonic oceanic crust during the Red Sea rifting (Tihama Asir igneous complex, Saudi Arabia)

***Basch V.[1], Sanfilippo A.[1,2], Vigliotti L.[3], Langone A.[2], Rasul N.[4], Khorsheed M.[4], AlNomani S.[4], AlQutub A.[4] and Ligi M.[3]**

[1] Dipartimento di Scienze della Terra e dell'Ambiente, Università degli Studi di Pavia, Italy

[2] Istituto Geoscienze e Georisorse, CNR, Pavia, Italy

[3] Istituto di Scienze Marine, CNR, Bologna, Italy

[4] Center for Marine Geology, Saudi Geological Survey, Jeddah, KSA

***Corresponding author:** Basch Valentin valentin.basch@gmail.com Dipartimento di Scienze della Terra e dell'Ambiente, Università di Pavia Via Ferrata 1, 27100 Pavia, Italy

**Abstract:**

The Red Sea rift system represents a key case study of the transition from a continental to an oceanic rift. The Red Sea rifting initiated in Late Oligocene – Early Miocene (~24-23 Ma) and was accompanied by extensive magmatism throughout the rifted basin, from Afar and Yemen to northern Egypt. Here, we present a petrological and geochemical study of two gabbro bodies and associated basalts from the Tihama Asir igneous complex, which formed at ~24-20 Ma within the rifted Arabian-Nubian Shield. The Tihama Asir is therefore an ideal location to study the initial phase of syn-rift magmatism and its influence on the geodynamic evolution of the Red Sea rift system. The most primitive olivine gabbros present modal, bulk and mineral compositions consistent with formation from MORB-type parental melts, whereas the evolved olivine-free gabbros and oxide-bearing gabbros show saturation of phlogopite and a crystal line of descent diverging from fractional crystallization trends. In detail, whole-rock and mineral compositions in the most evolved lithologies show high LREE/MREE ratios ($La_N/Sm_N$=0.89-1.31) and selective enrichments in Sr, K and highly incompatible elements (Rb, Ba, U, Th). We relate these geochemical characteristics to a process of progressive assimilation of host continental crust during the emplacement of the gabbroic plutons. Interestingly, high LREE/MREE ratios ($La_N/Sm_N$ = 1.45-4.58) and high Rb, Ba, Th, U contents also characterize the basaltic dike swarms associated to the gabbros. Incompatible trace element compositions of these basalts approach those of the melts that formed the most hybridized gabbros. Therefore, we propose that the dike swarms represent melts partially contaminated by assimilation of continental crust material, extracted from the underlying gabbroic crystal mush. Our results suggest that early syn-rift magmatism led to the partial replacement of the thinned continental crust by MORB-type gabbroic bodies, in turn suggesting that oceanic magmatism started prior to continental break-up. Extensive syn-rift magmatism is consistent with the interpretation of the southern Red Sea rift system as a volcanic rifted margin. One possible implication of this study is that extensive but diffuse syn-rift magmatism possibly hampered continental break-up, leading to a protracted rifting stage.

**Keywords:** *Red Sea rift system; Rift-to-drift history; MORB magmatism; Continental crust assimilation; Assimilation-Fractional Crystallization.*

## 1. INTRODUCTION

Continental break-up and the transition from rifting to oceanic drifting is a fundamental part of the Wilson plate tectonic cycle. However, the relative contribution of the different forces driving break-up of the continental lithosphere, e.g., active mantle convection upwelling or far-field plate separation forces, is still a matter of debate (e.g., Milanovsky, 1972; Burke & Dewey, 1973; Burke, 1996; Bosworth *et al.*, 2005; Moucha & Forte, 2011; Faccenna *et al.*, 2013; Almalki *et al.*, 2015; Bosworth, 2015; Ligi *et al.*, 2012, 2018; Stern & Johnson, 2019; Petrunin *et al.*, 2020). It was first suggested that the most common mode of continental rupture involves the formation of a rift triple junction triggered by active upwelling of deep-seated mantle material (Burke & Dewey, 1973). Accordingly, the Afar region and its associated rift system have been used as a reference case study to unravel the mechanisms of plate separation and continental break-up (e.g., Lowell & Genik, 1972; Almalki *et al.*, 2015).

Yet, no consensus has been reached regarding the tectonic evolution and the development of the Red Sea. The proposed models differ in the extent and distribution of oceanic crust, and several models have been proposed regarding the timing of continental breakup. Most models propose a recent onset of seafloor spreading in the southern Red Sea (~5 Ma; e.g., Courtillot, 1982; Cochran, 1983; Bonatti, 1985), whereas recent contributions infer earlier spreading of oceanic crust both in the southern and northern Red Sea (~13 Ma; e.g., Augustin *et al.*, 2021). Nonetheless, the different tectonic models concur on the initiation of the Red Sea rift in Late Oligocene – Early Miocene (~24-23 Ma). An intense phase of volcanism and magmatism appeared nearly synchronously throughout the entire rifted basin, from Afar and Yemen to northern Egypt (e.g., Pallister *et al.*, 1987; Chazot *et al.*, 1998; Bosworth *et al.*, 2005; Almalki *et al.*, 2015; Bosworth & Stockli, 2016; Abu El-Rus & Rooney, 2017; Sanfilippo *et al.*, 2019; Stern & Johnson, 2019), and led to the formation of basaltic dikes, layered gabbros and granophyre bodies (e.g., Coleman et al., 1975; Coleman, 1984; Bosworth & Stockli, 2016; Stern & Johnson, 2019). Volcanic activity was accompanied by extensive faulting and deposition of syn-rift marine sediments, thus marking the birth of the Red Sea rift (e.g., Bosworth et al., 2005).

In this contribution, we focus on the Tihama Asir in Saudi Arabia, a magmatic complex formed during the initial phase of Red Sea rifting (~24-20 Ma, e.g., Coleman *et al.*, 1972, 1975, 1979; Coleman, 1984; Sebai *et al.*, 1991; Bosworth & Stockli, 2016; Stern & Johnson, 2019). The Tihama Asir is a key location to study the initial phase of syn-rift magmatism and its influence on the geodynamic evolution of the Red Sea rift system. We combine textural

observations with whole-rock and mineral major and trace element compositions of gabbros and the associated dike complex to define the chemical evolution of the magmas that crystallized this crustal sequence and discuss the conditions of emplacement. We show that although the overall textures and major element compositions are similar to the gabbros exposed at mid-ocean ridges, trace element whole-rock and mineral compositions of evolved gabbros and basalt dikes reveal selective enrichments in elements having strong affinity with continental crust material (i.e., Ba, Th, U, K, Sr and LREE). Geochemical models of fractional crystallization associated with the assimilation of continental crust material successfully reproduce the selective enrichment in these elements. We infer that MORB-type magmatism associated with asthenosphere upwelling initiated before continental rupture, forming a transitional oceanic crust extensively hybridized by crustal contamination.

## 2. GEOLOGICAL SETTING

### 2.1. Geodynamic evolution of the Red Sea rift system

The Red Sea is a relatively narrow basin (~200-300 km-wide) extending from the junction of the Gulf of Suez and Gulf of Aqaba in the northwest (28°N, 34°E) and the Gulf of Aden and Afar to the southeast (13°N, 44°E; Fig. 1a). This modern rift system formed in response to the extensional forces related to the Zagros subduction slab pull and to the Afar plume asthenospheric upwelling (e.g., Bellahsen *et al.*, 2003; Almalki *et al.*, 2015; Bosworth, 2015; Kendall & Lithgow-Bertelloni, 2016; DeMets & Merkouriev, 2016; Petrunin *et al.*, 2020). The rift system separates the Nubian and Arabian Plates since the Late Oligocene-Early Miocene (e.g., Bosworth *et al.*, 2005; Stern & Johnson, 2010; Mohriak & Leroy, 2013; Bosworth, 2015; Bosworth & Stockli, 2016; Ligi *et al.*, 2019). This area is known as a key case study for a fundamental aspect of the Wilson cycle and plate tectonics, i.e., how continental lithosphere first breaks and evolves to oceanic spreading (also called *rift-to-drift* history). However, the models of tectonic evolution of the Red Sea strongly differ in the distribution and extent of oceanic crust inferred along the basin (e.g., Augustin *et al.*, 2021). Major discrepancies in the interpretation of the geophysical data (gravity, magnetism) from the northern Red Sea are caused by a thick sedimentary cover and extensive salt deposits hindering the underlying basement and producing unusual geophysical signatures (e.g., Levi & Riddihough, 1986). Some studies suggest that the main phases of evolution from continental rifting to oceanic drifting coexist in the Red Sea rift system, from a mature

oceanic crust in the Gulf of Aden and southern Red Sea to an active continental rift system in the northern Red Sea and in the Gulf of Suez (e.g., Phillips, 1970; Girdler & Styles 1974; Röser, 1975; Searle & Ross, 1975; Hall *et al.*, 1977; Cochran, 1983, 2005; Bonatti, 1985; Zahran *et al.*, 2003; Stern & Johnson, 2010; Lazar *et al.*, 2012; Ligi *et al.*, 2012, 2018, 2019; Almalki *et al.*, 2015; Bosworth, 2015; Bosworth *et al.*, 2020). Other studies proposed a more mature stage of evolution of the basin, with continuous oceanic spreading occurring throughout the whole Red Sea basin (e.g., Sultan *et al.*, 1992; Ghebreab, 1998; Augustin *et al.*, 2014, 2021).

A general agreement exists on the initial stages of evolution of the Red Sea rift system, that can be summarized as follows: *i)* plume-related basaltic magmatism began in Ethiopia and southwestern Yemen at ~31 Ma, followed by rhyolitic volcanism at ~30 Ma (Fig. 1a; e.g., Mattash *et al.*, 2014; Bosworth & Stockli, 2016; Stern & Johnson, 2019); *ii)* continental rifting and syn-tectonic marine sedimentation initiated in the central Gulf of Aden between ~30 Ma and 28.7 Ma (Roger *et al.*, 1989; Hughes *et al.*, 1991; Watchorn *et al.*, 1998; Bosworth *et al.*, 2005); *iii)* an initial Red Sea rift basin formed offshore Eritrea by ~27-24 Ma (Hugues *et al.*, 1991; Bosworth *et al.*, 2005). Simultaneously (~25 Ma, Late Oligocene), extension and rifting commenced within Afar itself (Barberi *et al.*, 1972, 1975; Bosworth *et al.*, 2005); *iv)* a new phase of volcanism appeared nearly synchronously throughout the entire Red Sea rift basin at ~24-23 Ma (Late Oligocene – Early Miocene). The latter volcanism was accompanied by extensive faulting (e.g., Bosworth *et al.*, 2005 and references within) and extended from Afar and Yemen to northern Egypt, forming basaltic dikes, layered gabbros and granophyre bodies (Fig. 1a, b; e.g., Coleman *et al.*, 1975; Coleman, 1984; Bosworth & Stockli, 2016; Stern & Johnson, 2019). *v)* after 12 Ma of continental rifting (from ~31 Ma to ~19-18 Ma), the lithosphere was sufficiently thinned to allow for the rift-to-drift transition and the establishment of an oceanic spreading centre in the eastern part of the Gulf of Aden (Sheba Ridge; Sahota, 1990; Leroy *et al.*, 2004). Oceanic spreading propagated westwards into the central Gulf of Aden by ~16 Ma (Bosworth, 2015), reached the Shukra El-Sheik fracture zone at ~10 Ma (Manighetti *et al.*, 1997) and propagated into Afar at ~8 Ma (e.g., Audin *et al.*, 2004).

### 2.2. Tihama Asir igneous complex

The present study focuses on the Tihama Asir igneous complex, located in southwestern Saudi Arabia, east of the Jizan coastal plain (Fig. 1). This complex is composed of different

gabbroic bodies that preserve primary contacts with irregular granophyre plutons. The Tihama Asir igneous complex intruded the strongly faulted Arabian Shield Neoproterozoic basement. The gabbros and granophyres are physically associated with dike swarms ranging in composition from basalts to rhyolites. McGuire & Coleman (1986) reported that the gabbros and granophyre bodies crosscut the associated dike swarm, the earliest intrusions from the igneous complex (Fig. 2a), but that dike formation continued throughout the formation of the Tihama Asir. The dikes preserve intrusive contacts with the continental basement, here including amphibolite-grade tholeiitic basalts, rhyolites, kyanite-muscovite-quartzite, schists, and abundant biotite granite-gneiss (Fig. 1b; Fig. 2a; e.g., Coleman *et al.*, 1979; Blank & Gettings, 1984; Coleman & McGuire, 1986; McGuire & Coleman, 1986; Hegner & Pallister, 1989; Stern & Johnson, 2019). K-Ar dating indicates a Late Oligocene – Early Miocene (~24.3-20.0 Ma) age of formation for the Tihama Asir igneous complex and dike swarms (Coleman *et al.*, 1972, 1975, 1979; Coleman, 1984; Sebai *et al.*, 1991; Bosworth & Stockli, 2016), which are therefore coeval with the initial phase of rifting and with the formation of the widespread syn-rift volcanism in the western Arabian Plate (Amalki *et al.*, 2015; Bosworth, 2015; Stern & Johnson, 2019). The tectonic history of the Jizan coastal plain was dominated by a SW-NE extension documented by several generations of NW-SE normal faults (Bohannon, 1986; McGuire & Coleman, 1986) and the oldest syn-rift deposits marked by non-marine sediments and volcanics of the Baid formation (Jizan Group, Schmidt *et al.*, 1982). The lacustrine laminites of the Jizan Group were intruded by dikes, gabbros and granophyres of the Tihama Asir magmatic complex (Coleman *et al.*, 1979, Bohannon, 1986; McGuire & Coleman, 1986; Voggenreiter *et al.*, 1988).

Based on whole-rock analyses of granophyres and few layered gabbros from the Jabal al Tirf pluton (Fig. 1b), McGuire & Coleman (1986) documented a tholeiitic affinity of the parental magmas. Notably, they suggested that a process of continental crust assimilation triggered chemical differentiation of the basaltic magmas towards granitic compositions, thereby leading to the formation of the granophyres. In this contribution, we extend the petrological and geochemical characterization to 5 gabbros from Jabal al Tirf, and further expand our analyses to 12 gabbros and 2 basalts from the Masliyah pluton and 12 basalts from the Jabal Sawdah dike swarm (Fig. 1b).

Jabal al Tirf is located ~40 kilometres east of Jizan (Fig. 1b, Fig. 2a) and consists of a well-exposed layered gabbro body (~2 km-wide, ~8 km-long) striking northwest, parallel to the Red Sea axis. The gabbros show a metre-scale compositional layering defined by modal variations of olivine, plagioclase, clinopyroxene and Fe-Ti oxide. This metre-thick

compositional layering dips towards the west (e.g., McGuire & Coleman, 1986; Stern & Johnson, 2010, 2019). The magmatic layering disappears gradually up-section, where the gabbros are mostly isotropic, especially at the contact with the granophyre intrusion capping Jabal al Tirf (Fig. 2a, b). This contact is characterized by a 30-metre-thick zone of thermal alteration.

The Masliyah pluton is located ~60 kilometres north of Jizan and consists of layered gabbros showing a metre-scale compositional layering locally associated with magmatic foliation. Similar to the Jabal al Tirf pluton, the layered gabbro sequence is capped by a granophyre intrusion. The layered gabbros are crosscut by fine-grained gabbros showing porphyric textures (see later for more detail) and fine-grained basalt dikes, both ranging from 0.5 to 19 metres in thickness (Fig. 2c). Porphyric gabbros are more common in the upper part of the gabbroic body and show no chilled margins at the contact with the host rock. Jabal Sawdah, located in the north-western part of the Tihama Asir igneous complex (Fig. 1b), exposes a well-developed dike swarm, coeval with the gabbros and mostly constituted of diabase dikes striking NNW-SSE, thus parallel to the present-day Red Sea axis. Field observations indicate that the dike swarm intruded the metamorphic basement and granites of the Neoproterozoic Arabian Shield (Fig. 2a, d; e.g., Coleman & McGuire, 1986; McGuire & Coleman, 1986; Stern & Johnson, 2010, 2019). The field relationships between the Masliyah and the Jabal Sawdah dike swarm are hindered by quaternary sediments within the Wadi Baysh (Fig. 1b), but the association between gabbroic bodies and dike swarms is commonly described along the Arabian margin (e.g., Coleman *et al.*, 1979; Pallister,1987; Stern & Johnson, 2019).

## 3. SAMPLE SELECTION AND ANALYTICAL METHODS

In this study, we investigated 29 samples including gabbros and basalts collected in different locations of the Tihama Asir igneous complex (see Table 1). The samples from the Masliyah and the Jabal al Tirf plutons (12 and 5 samples, respectively) include 5 olivine gabbros (Ol > 5 vol%), 5 cpx-gabbros (Ol < 5 vol%), 1 oxide gabbro (Fe-Ti oxide > 10 vol%), 4 “porphyric” gabbros and 2 isolated basaltic dikes crosscutting the gabbros with sharp contacts and chilled margins (Fig. 2b, c; see *Petrography* for detailed description). The samples from the Jabal Sawdah dike swarm consist of 12 basaltic dikes crosscutting the continental basement (Fig. 2d).

Internal portions of gabbroic and basaltic rocks were crushed and pulverized in a tungsten carbide swing mill and measured for whole rock major and trace element concentrations using ICP-mass spectrometry at Activation Laboratories Ltd. (Ancaster, Ontario). Total analytical errors of the element analyses are within 10%. Details of the analytical techniques and detection limits are available from the company website (www.actlabs.com). Loss on Ignition (LOI) was defined by measuring the difference in mass of the powdered samples before and after being heated to 1000°C for twelve hours in a chamber furnace. The $Fe_2O_3$ content of the whole-rock analyses has been converted to FeO using a conversion factor of 0.8998.

Mineral major and trace element analyses were performed on 6 samples, including 2 olivine gabbros, 2 cpx-gabbros, 1 oxide gabbro and 1 porphyric gabbro.

Major element ($SiO_2$, $TiO_2$, $Al_2O_3$, $Cr_2O_3$, FeO, MgO, MnO, CaO, NiO, $Na_2O$, $K_2O$) compositions of clinopyroxene, plagioclase, amphibole, olivine and biotite were analysed by a JEOL JXA 8200 Superprobe equipped with five wavelength-dispersive (WDS) spectrometers, an energy dispersive (EDS) spectrometer, and a cathodoluminescence detector operating at the Dipartimento di Scienze della Terra, University of Milano, Italy. The analyses of all elements were performed with a 1 µm spot size, 30-seconds counting time at an accelerating potential of 15 kV and a beam current of 15 nA. Natural oxides were used as standards and the quality of analyses was assessed on the basis of the atom per formula units.

Trace element compositions of clinopyroxene, plagioclase and amphibole were determined by Laser Ablation-Inductively Coupled Plasma-Mass Spectrometry (LA-ICP-MS) at CNR, Istituto di Geoscienze e Georisorse (Unità di Pavia). We used a PerkinElmer SCIEX ELAN DRC-e quadrupole mass spectrometer coupled with an UP213 deep-UV YAG Laser Ablation System (New Wave Research, Inc.). Laser (213nm wavelength) spot size was set to 100µm and the ablation frequency to 10 Hz, with a fluence of ~9.5 J/cm$^2$. Helium was used as the carrier gas and was mixed with Ar downstream from the ablation cell. Data reduction was performed using the GLITTER software. NIST SRM 610 synthetic glass was used as the external standard, and CaO concentrations previously measured by EPMA were used as the internal standard. The precision and accuracy of the trace element concentrations were assessed by repeated analyses of the BCR2-g standard and were better than ±7% and ±10%, respectively.

## 4. PETROGRAPHY

*Olivine gabbros* show a hypidiomorphic texture of submillimetric to millimetric olivine (8-21 vol%), plagioclase (50-55 vol%), clinopyroxene (26-35 vol%), Fe-Ti oxide (1-7 vol%) and rare brown amphibole (0-3 vol%) (Fig. 3a, b; Table 1). Some samples display millimetre-scale variations in modal composition characterized by alternation of layers rich in euhedral olivine, and layers rich in clinopyroxene and Fe-Ti oxide (Fig. 3a). Plagioclase laths often define a weak foliation parallel to the elongation of the plagioclase crystals (Fig. 3b). The latter commonly show intra-crystalline deformation features such as bending, mechanical twins and undulose extinctions (Fig. 3b), and locally display serrate contacts between plagioclase crystals, resulting in crystal interlocking (Fig. 3b; e.g., Ferrando *et al.*, 2021a). Undeformed clinopyroxene oikocrysts commonly include euhedral plagioclase and olivine chadacrysts. Fe-Ti oxide is found to be either euhedral in clinopyroxene-rich layers (Fig. 3a) or interstitial to poikilitic, including euhedral plagioclase and clinopyroxene chadacrysts. Fe-Ti oxides are in places associated with interstitial brown amphibole (Table 1).

*Cpx-gabbros* show a similar hypidiomorphic texture to the olivine gabbros, with submillimetric to millimetric plagioclase (52-72 vol%), clinopyroxene (20-40 vol%), Fe-Ti oxide (5-10 vol%), rare amphibole (1-2 vol%), olivine (0-2 vol%) and orthopyroxene (0-5 vol%) (Fig. 3c, d; Table 1). A weak foliation is defined by the elongation of deformed plagioclase laths (Fig. 3c). Euhedral plagioclase chadacrysts are often found included in poikilitic clinopyroxene or Fe-Ti oxide, the latter being commonly associated with interstitial amphibole (Fig. 3c). Subhedral millimetre-size orthopyroxene is commonly associated with clinopyroxene and minor plagioclase, forming centimetre-scale gabbronoritic to websteritic aggregates (Fig. 3d).

The *oxide gabbro* is characterized by millimetre-size plagioclase (40 vol%), clinopyroxene (35 vol%), Fe-Ti oxide (16 vol%), minor olivine (4 vol%) and rare amphibole (1 vol%). Its most distinctive characteristic is the presence of discrete quantities of interstitial dark mica (4 vol%). The latter is often associated with interstitial Fe-Ti oxide (Fig. 3e; Table 1). Clinopyroxene is poikilitic and shows brown amphibole patches often aligned along the exsolution lamellae (Fig. 3e).

*Porphyric gabbros* are characterized by millimetre- to centimetre-scale aggregates of euhedral plagioclase glomerocrysts (up to 40 vol%) embedded in a microcrystalline matrix of plagioclase + clinopyroxene + Fe-Ti oxide showing subophitic textures (Fig. 3f; Table 1). The texture of this lithotype is similar to porphyritic basalts but shows a fully crystalline matrix (>100 μm grain size); we therefore refer to these samples as porphyric gabbros. Sample TA01-Tlg1 includes a sharp but irregular contact between a porphyric gabbro and a

basaltic dike, the latter presenting chilled margins at its contact with the porphyric gabbro (Fig. 3f).

*Basaltic dikes*, from both Masliyah and Jabal Sawdah, show 10 to 20 vol% of plagioclase phenocrysts embedded in a microcrystalline matrix (80-90 vol%; Table 1). The dikes often show chilled margins at the contact with the host rock, suggesting emplacement in a brittle environment and rapid cooling (e.g., Huppert & Sparks, 1989; Hayman *et al.*, 2009).

## 5. CHEMISTRY

### 5.1. Whole rock major and trace element compositions

#### *5.1.1. Tihama Asir gabbros*

The studied gabbroic samples from the Tihama Asir igneous complex show a large whole-rock compositional variability, ranging from high Mg-numbers (Mg# = Mg/[Mg+Fe] mol%) in olivine gabbros (Mg# = 59.7-70.6) to progressively lower Mg-numbers in cpx-gabbros (Mg# = 53.9-61.8), porphyric gabbros (Mg# = 55.5-57.7) and oxide gabbros (Mg# = 40.4) (Fig. 4; Supplementary Table S1). Selected samples are characterized by LOI < 3 wt% and show relatively homogeneous concentrations of CaO (11.4-14.9 wt%; Fig. 4a) and $Na_2O$ (2.05-2.59 wt%). Although the compositions of the different lithotypes overlap, the studied gabbroic samples define compositional trends defined by covariations between Mg-numbers, major and trace elements and fall in the compositional range defined by mid-ocean ridge gabbros (Godard *et al.*, 2009). For instance, olivine gabbros tend to show lower concentrations of $TiO_2$ (0.41-1.14 wt%), $K_2O$ (0.06-0.18 wt%; Fig. 4b) and higher concentrations of Ni (60-90 ppm) and Cr (300-690 ppm) with respect to cpx-gabbros ($TiO_2$ = 0.57-1.27 wt%; $K_2O$ = 0.13-0.22 wt%; Ni = 30-60 ppm; Cr = 20-280 ppm), porphyric gabbros ($TiO_2$ = 0.84-0.96 wt%; $K_2O$ = 0.19-0.25 wt%; Ni = 40-50 ppm; Cr = 60-100 ppm) and the oxide gabbro ($TiO_2$ = 2.95 wt%; $K_2O$ = 0.28 wt%; Ni = 80 ppm; Cr = <20 ppm).

Whole-rock incompatible trace element abundances of the Tihama Asir gabbros (Supplementary Table S1) show negative correlations with Mg-numbers. The concentrations of REE-Y and other incompatible trace elements (Fig. 4) overlap considerably between the different lithotypes, but show an overall increase from the most primitive olivine gabbros (e.g., La = 0.83-2.67 ppm; Y = 6.6-19.1 ppm; Sr = 165-260 ppm; Nb = <0.2-3.0 ppm; U = 0.02-0.08 ppm) to the cpx-gabbros (La = 2.15-4.27 ppm; Y = 10.6-27.6 ppm; Sr = 199-282 ppm; Nb = 1.8-3.8 ppm; U = 0.07-0.09 ppm), the porphyric gabbros (La = 3.15-5.97 ppm; Y

= 17.0-22.3 ppm; Sr = 219-233 ppm; Nb = 3.0-5.8 ppm; U = 0.12-0.21 ppm) and the oxide gabbro (La = 4.26 ppm; Y = 19.3 ppm; Sr = 190 ppm; Nb = 3.5 ppm; U = 0.16 ppm).

The CI-normalised REE patterns of the Tihama Asir gabbros show variations both in terms of absolute concentrations and LREE/HREE fractionation. Olivine gabbros show the lowest REE concentrations ($Yb_N$ = 3.26-11.82 times CI chondrite; Fig. 5a) and relatively flat REE-Y patterns ($La_N/Y_N$ = 0.71-0.93; Fig. 4e). Selective enrichments in LREE and Sr are observed in the cpx-gabbros ($Yb_N$ = 6.03-16.92 times CI chondrite; $La_N/Y_N$ = 0.87-1.47), porphyric gabbros ($Yb_N$ = 9.42-12.55 times CI chondrite; $La_N/Y_N$ = 1.03-1.77) and oxide gabbro ($Yb_N$ = 10.58 times CI chondrite; $La_N/Y_N$ = 1.46). A pronounced Ti positive anomaly characterizes the oxide gabbro, consistent with accumulation of Fe-Ti oxides (Fig. 5b; Table 1).

### *5.1.2. Tihama Asir basalts*

The studied basalts are characterized by more evolved compositions than the gabbros overall and show extensive whole-rock compositional variability (Supplementary Table S1), with higher Mg-numbers for the metre-scale dikes crosscutting the gabbros in the Masliyah pluton (Mg# = 45.4-58.2; "*crosscutting dikes*" in the following) with respect to the dike swarm exposed at Jabal Sawdah (Mg# = 28.6-52.5; *"dike swarm"* in the following) (Fig. 4). Basalt dikes are characterized by LOI ranging from 0.1 to 4 wt%. Taken as a whole, major and minor element compositions of the basaltic dikes define positive correlations between Mg-number and elements showing high affinity with olivine, plagioclase and clinopyroxene, such as CaO (6.2-10.5 wt%; Fig. 4a), $Al_2O_3$ (11.8-18.7 wt%), Ni (30-50 ppm) and Cr (20-90 ppm), and negative correlations between the Mg-number and incompatible elements such as $K_2O$ (0.58-2.19 wt%; Fig. 4b), $TiO_2$ (1.15-2.46 wt%) and $P_2O_5$ (0.17-0.44 wt%). Whole-rock trace element contents of the Tihama Asir basalts are also overall higher than the gabbros and tend to increase at decreasing Mg-number (e.g., La = 8.42-26.50 ppm; Y = 26.1-81.6 ppm; Sr = 173-538 ppm; Nb = 8.7-23.6 ppm; U = 0.35-1.45 ppm; Fig. 4; Supplementary Table S1).

The CI-normalised REE patterns of the crosscutting dikes and dike swarm show strong differences in LREE/HREE fractionation. The crosscutting dikes have relatively flat REE-Y patterns ($La_N/Y_N$ = 1.05-1.26; Supplementary Table S1), whereas basalts from the dike swarm show strongly variable LREE/HREE-Y fractionation with $La_N/Y_N$ ratios ranging from

1.70 to 4.18, progressively increasing at increasing REE absolute concentration (Supplementary Table S1).

### 5.2. Mineral major and trace element compositions

*Clinopyroxenes* from the Tihama Asir gabbros (Supplementary Table S2) show Mg-numbers ranging from 57.7 to 78.0, variable $TiO_2$ (0.48-0.92 wt%; Fig. 6a) and $Cr_2O_3$ (0.01-0.30 wt%; Fig. 6b), following the compositional trend of clinopyroxene from the mid-ocean ridge gabbros from the Atlantis Massif (Miller *et al.*, 2009). Clinopyroxene incompatible trace element contents show negative correlations with Mg-numbers. Clinopyroxenes from the olivine gabbros show more primitive compositions than the clinopyroxenes from the cpx-gabbros, which in turn show very strong compositional variability (Fig. 7,8). Notably, most clinopyroxenes show chemical zoning defined by primitive crystal cores and gradually evolved crystal rims. The whole range of trace element variability defined by a given lithotype can be found within a single sample (Fig. 7; Fig. 8a, b; Supplementary Table S2). At increasing $Yb_N$, clinopyroxenes from all lithologies show a progressive increase in $La_N$ (0.58-7.13 times Primitive Mantle; Fig. 7a), LREE/HREE-Y ($La_N/Y_N$ = 0.17-0.78; Fig. 7b; Fig. 8b) and LREE/MREE ratios ($La_N/Sm_N$ = 0.17-0.64; Fig. 7c; Fig. 8a, b). These increases are coupled with selective enrichments in highly incompatible elements (e.g., $Th_N/Y_N$ = 0.04-0.97; Fig. 7d; Fig. 8b). Clinopyroxene REE patterns also show progressive increase of the Eu and Sr negative anomalies at increasing $Yb_N$ (Eu/Eu* = 0.51-1.19; Sr/Sr* = 0.05-0.38; Fig. 8a).

*Plagioclases* from the Tihama Asir gabbros (Supplementary Table S3) show anorthite contents ranging from 44.7 to 65.1 mol%; the latter are positively correlated with the Mg-number in coexisting clinopyroxenes (Fig. 6c), following the compositional trend defined by the Mid-Atlantic ridge gabbros (Miller *et al.*, 2009). Plagioclase REE and incompatible trace element patterns show selective enrichments in LREE and highly incompatible elements (e.g., Rb, Ba, Th, U, Ta, K) with respect to HREE concentrations (Fig. 8c, d). Similar to clinopyroxene, the plagioclase LREE/HREE fractionation increases at increasing HREE absolute concentrations ($La_N/Y_N$ = 6.7-180.5; Fig. 8c, d; Supplementary Table S3). Plagioclases within the oxide gabbro show the highest concentrations of LREE and highly incompatible elements (e.g., $La_N$ = 4.94-19.05 times CI chondrite; Fig. 8c, d), and the most fractionated REE patterns ($La_N/Y_N$ = 20.5-180.5; Fig. 8c, d). Similar to clinopyroxene, strong geochemical zoning is observed between plagioclase cores and rims, which in a single sample

can cover most of the trace element compositional variability observed in plagioclases from a given lithotype of the Tihama Asir gabbros (Supplementary Table S3).

*Brown amphiboles* from the Tihama Asir olivine and cpx-gabbros (Supplementary Table S4) show Ti-pargasitic compositions (following classification from Leake *et al.*, 1997). Major element compositions are rather uniform between the different lithologies ($SiO_2$ = 42.42-44.19 wt%; $TiO_2$ = 2.80-3.64 wt%; $Al_2O_3$ = 9.35-10.29 wt%; $Na_2O$ = 2.44-2.54 wt%; $K_2O$ = 0.60-0.86 wt%). Amphiboles are characterized by high REE and trace element contents ($La_N$ = 9.2-44.9 times Primitive Mantle; $Y_N$ = 10.0-26.5 times Primitive Mantle; Fig. 8e,f), and relatively flat REE-Y patterns ($La_N/Y_N$ = 0.9-2.5; Fig. 8e,f). Similar to clinopyroxene and plagioclase, the amphibole shows an increase in LREE/M-HREE fractionation and negative Eu and Sr anomalies (Eu/Eu* = 0.40-0.95; Sr/Sr* = 0.04-0.28; Fig. 8f) at increasing REE concentrations. In addition, brown amphiboles show high Nb absolute concentrations ($Nb_N$ = 19.6-28.1 times Primitive Mantle; Fig. 8f), consistent with a magmatic origin (Coogan *et al.*, 2001).

*Olivines* from the Tihama Asir olivine and cpx-gabbros (Supplementary Table S5) show forsterite contents (Fo = Mg/[Mg+Fe]) ranging from 56.5 to 68.5, positively correlated with olivine NiO compositions (NiO = 0.028-0.057 wt%; Fig. 6d) and clinopyroxene Mg-numbers.

*Dark micas* from the oxide gabbro (Supplementary Table S6) are characterized by phlogopitic compositions ($Al_2O_3$ = 13.45-13.83 wt%; $TiO_2$ = 5.85-5.87 wt%; FeO = 13.70-13.89 wt%; MgO = 15.08-15.21 wt%; $K_2O$ = 8.73-8.77 wt%; e.g., Fleet, 2003; Nachit *et al.*, 2005).

## 6. DISCUSSION

The Tihama Asir igneous complex is arguably one of the best exposed examples of a syn-rift crustal sequence in the western Arabian margin (Fig. 1a; e.g., Bosworth & Stockli, 2016; Stern & Johnson, 2019). However, since the pioneering works of Coleman & McGuire (1986) and McGuire & Coleman (1986), no detailed petrological investigation of this magmatic complex has been conducted. In this framework, this study provides a thorough petrological investigation of the Tihama Asir igneous complex and allows for a detailed assessment of the previously inferred and alternative magmatic processes, as well as their implication on the geodynamic evolution of the Red Sea rift system.

The melts erupted in the Arabian peninsula during Cenozoic times are characterized by variable geochemical affinities spanning from (high-Na) alkaline to tholeiitic (e.g., Amalki *et al.*, 2015; Bosworth & Stockli, 2016; Sanfilippo *et al.*, 2019; Stern & Johnson, 2019). Thus, before making any inference on the magmatic processes that led to the formation of the studied gabbroic bodies, we will first define the affinity of the melts parental to the Tihama Asir igneous complex.

### 6.1. Geochemical affinity of the Tihama Asir igneous complex parental melts

In their pioneering studies, Coleman & McGuire (1986) and McGuire & Coleman (1986) used petrological and chemical data of granophyres and layered gabbros from Jabal al Tirf to argue that the Tihama Asir igneous complex formed from parental magmas with a tholeiitic affinity, akin to modern MORB. They inferred that the granophyres formed after a process of continental crust assimilation that triggered chemical differentiation of basaltic magmas towards granitic compositions. Consistently, geochemical investigations of syn-rift gabbroic bodies from the northern Red Sea argued that the emplacement of mafic complexes with a tholeiitic affinity anticipated continental break-up and the onset of seafloor spreading (e.g., Ligi *et al.*, 2018). They suggested that MORB-type melts intruded the thinned continental crust already during initial stages of the Red Sea rift extension (e.g., Bonatti & Seyler, 1987; Bonatti *et al.*, 2015; Ligi *et al.*, 2012, 2018, 2019). Ligi *et al.* (2018) documented that the syn-rift MORB-type intrusions in the northern Red Sea (~22 Ma) occurred at variable depths within the continental crust; they reported deep gabbroic intrusions (emplaced at 8-9 kbar) in the Zabargad Island gabbros and shallower gabbroic intrusions (2.5-3.5 kbar) in the QUSEIR B-1X oil well and in the Brothers Islands (see Fig. 1a). Additionally, MORB-type gabbros have been recently documented along the Red Sea axis at Discovery Deep (21°N) and show undistinguishable compositions from abyssal gabbros recovered in the Atlantic and Indian oceans (Follmann *et al.*, 2021). Consistent with a tholeiitic affinity of the parental melts to the Tihama Asir igneous complex, the most primitive olivine gabbros from our sample suite show bulk-rock major and trace element compositions that fall within the compositional field of mid-Atlantic ridge gabbros (Fig. 4; Godard et al., 2009). We note that E-MORB to OIB-type incompatible trace element patterns are locally found in MORB glasses sampled at 17°N along the Red Sea axis and possibly related to the influence of enriched material from the Afar plume in their mantle source (e.g., van der Zwan *et al.*, 2015). Yet, although enriched material from the Afar might have influenced the asthenospheric source at these latitude, this

does not preclude the tholeiitic affinity of the parental melts of the Tihama Asir gabbros (see further discussion in Section 6.3). Isotopic data on our sample suite will shed light on the possible role of the Afar in their mantle source and will be detailed in a separate contribution. The most primitive olivine gabbros also show REE and trace element patterns similar to the Brothers and QUSEIR gabbros (Fig. 5a,b; referred to as "*Red Sea gabbros*" in the figures and in the following), sustaining the idea that all the syn-rift gabbroic intrusions in the Red Sea rift system formed from tholeiitic parental melts produced by an asthenospheric mantle source (see also Ligi *et al.*, 2018, 2019). Considering all the studied gabbroic samples, the bulk composition of olivine gabbros, cpx-gabbros, porphyric gabbros and oxide gabbro from the Tihama Asir igneous complex show a progressive increase in incompatible trace element contents (i.e., La, Y, Sr, Nb, U; Fig. 4) at decreasing Mg-numbers. The studied gabbros thereby depict a single crystal line of descent tracing a process of magmatic differentiation from primitive compositions in olivine gabbros to evolved compositions in oxide gabbros (Fig. 4; Fig. 5).

However, despite the primitive olivine gabbros from the Tihama Asir suggest crystallization from melts having a MORB-type affinity, the bulk-rock compositions of the more evolved gabbroic lithologies (i.e., cpx-gabbros, porphyric gabbros and the oxide gabbro) diverge from the compositional trend defined by the lower oceanic crust formed at mid-ocean ridges. The Tihama Asir evolved gabbros show selective enrichments in highly incompatible elements (e.g., $K_2O$, Sr, Nb, U; Fig. 4) and a progressive increase in LREE/HREE-Y fractionation, ranging from $La_N/Y_N$ = 0.71-0.93 in olivine gabbros to $La_N/Y_N$ = 1.03-1.77 in the porphyric gabbros (Fig. 5a, b). Enrichments in highly incompatible elements are also observed in clinopyroxene and plagioclase compositions (e.g., Rb, Ba, Th, U, LREE; Fig. 8b, d). These selective enrichments lead to a progressive increase in LREE/HREE fractionation, from $La_N/Y_N$ = 0.17 in the most primitive clinopyroxene to $La_N/Y_N$ = 0.61 in the most evolved ones, with a large range of variability locally found within a single sample (Fig. 7; Fig. 8a, b). Given small differences in the bulk partition coefficients of REE and Y in a gabbroic mineral association (i.e., olivine, plagioclase and clinopyroxene), such gradual variations in $La_N/Y_N$ are not expected during a simple process of fractional crystallization. Rather, additional processes need to be invoked to explain such enrichments, with profoundly different implications for the evolution of the magmatic system: *i)* diffusive reequilibration at sub-solidus conditions (e.g., Coogan & O'Hara, 2015); *ii) in situ* crystallization (e.g., Langmuir, 1989; Jenner & O'Neill, 2012; Coogan & Dosso, 2016); *iii)* mixing of different melt compositions (e.g., Coogan *et al.*, 2000; Cashman *et al.*, 2017;

Edmonds *et al.*, 2019), and *iv)* reactive crystallization (e.g., Sanfilippo *et al.*, 2014, 2020; Fischer *et al.*, 2016; Basch *et al.*, 2018; Ferrando *et al.*, 2018; Leuthold *et al.*, 2018; Lissenberg *et al.*, 2019; Rampone *et al.*, 2020). In the following, we assess these different processes and their ability to reproduce the incompatible trace element composition of the Tihama Asir gabbros.

### 6.2. Origin of the selective enrichments in highly incompatible elements

#### *6.2.1. Diffusive reequilibration*

*Diffusive reequilibration* has been documented as a process capable of significantly modifying mineral trace element compositions by element redistribution during progressive cooling (i.e., sub-solidus conditions). Moreover, since elements with different incompatibilities can migrate at different rates during cooling of a magmatic system, diffusion can generate significant changes in trace element compositions of minerals (i.e., chromatographic separation; Coogan & O'Hara, 2015). Such a process of intra- and inter-mineral elemental diffusion during sub-solidus reequilibration could lead to compositional zoning in minerals and to changes in the element ratios as a function of temperature. In order to assess the role of diffusive reequilibration in creating the trace element enrichments observed in minerals from the Tihama Asir gabbros, we computed the equilibrium temperature of the clinopyroxene-plagioclase mineral couples, using the REE geothermometer from Sun & Liang (2017). Couples of average clinopyroxene-plagioclase cores and rims within all lithologies yield equilibrium temperatures ranging from 1048°C to 1180°C (Fig. 9a), with rim couples showing slightly lower equilibrium temperatures than clinopyroxene-plagioclase cores (up to 50°C difference). This suggests that equilibration occurred at magmatic temperatures. In addition, diffusion is expected to cause a flux of HREE-Y from plagioclase into adjacent clinopyroxene, in turn generating a gradual modification in HREE-Y concentrations at decreasing temperature (Coogan & O'Hara, 2015). Figure 9a shows that the $Y_N$ concentrations in both plagioclase and clinopyroxene are nearly constant at decreasing equilibrium temperatures, implying that subsolidus diffusion of REE-Y between coexisting clinopyroxene and plagioclase did not substantially modify the trace element patterns of these minerals. Finally, subsolidus diffusion in a closed system cannot explain the gradual and selective enrichments in highly incompatible elements of the bulk-rock compositions, which rather require an open-system process. On this basis, we can

reasonably discard diffusive reequilibration as the driving process causing the selective bulk-rock and mineral enrichments in highly incompatible elements in the Tihama Asir gabbros.

### *6.2.2. In situ crystallization*

*In situ crystallization* has been invoked to explain enrichments in incompatible elements in minerals from continental layered intrusions (Langmuir, 1989) as well as in mid-ocean ridge basalts (Coogan & O'Hara, 2015). *In situ* crystallization involves crystallization at the margins of a magma chamber and subsequent return of the residual melt within the magma chamber interior, where it is mixed with new incoming melt. To assess the ability of this process to explain the incompatible trace element enrichments observed in the Tihama Asir minerals, we performed a model of "*in situ* crystallization" using the equation given by Langmuir (1989). We considered different amounts of residual melt returning into the magma chamber interior, from $f$ = 0.1 (strongly fractionated melt is mixed back into the magma chamber) to $f$ = 1 (corresponding to fractional crystallization). The starting melt composition has been computed in equilibrium with a clinopyroxene core from the most primitive olivine gabbro from the Tihama Asir, and partition coefficients have been taken from the compilation given by Basch *et al.* (2018). The modal composition of fractionated minerals has been computed at each step of 5°C cooling using the MELTS thermodynamic software (Ghiorso & Sack, 1995).

Figure 9b shows the composition of the clinopyroxene in equilibrium with the melt at variable $f$, considering a melt crystallizing from F = 1 to F = 0.2 (i.e., 20% of initial melt mass). The clinopyroxene in equilibrium with the computed melt shows progressive enrichments in highly incompatible elements at decreasing $f$, in turn leading to increasing LREE/HREE fractionation (i.e., $La_N/Y_N$; Fig. 9b). Regardless of the amount of residual melt returning into the magma chamber interior, the modeled incompatible trace element enrichments can reproduce only part of the clinopyroxene compositions analysed in the Tihama Asir gabbros ($La_N/Y_N$ <0.4), failing to explain the enriched compositions characterizing the most evolved lithologies.

### *6.2.3. Magma mixing*

*Mixing* processes are part of the fundamental processes driving the dynamics of magma chambers (e.g., Coogan & Dosso, 2016; Cashman *et al.*, 2017). Mixing between different melts (i.e. variably evolved melts or melts with different magmatic affinities) within a magma chamber can lead to drastic modifications in the composition of the crystallized mineral phases (e.g., Anderson, 1976; Cashman *et al.*, 2017; Edmonds *et al.*, 2019). Given that the Cenozoic magmatism in the western Arabian margin ranged from high-Na alkaline to tholeiitic (e.g., Sanfilippo *et al.*, 2019; Stern & Johnson, 2019), one could argue that mixing between parental melts with different trace element compositions might have produced the variations documented in the Tihama Asir gabbros. However, mixing of different parental melts would have caused a random distribution of enriched and depleted trace element signatures in the different lithologies, contrasting with the observation that the bulk-rock enrichments in elements with crustal affinity are more accentuated in the most evolved Tihama Asir gabbros.

Moreover, in-situ analyses of mineral phases reveal that such enrichments characterize preferentially the evolved clinopyroxene rims, with clinopyroxene in single samples locally spanning the entire geochemical variability of all gabbros in a single lithology (Fig. 7; Fig. 8a, b). These features indicate that the process responsible for the enrichments in highly incompatible trace elements was progressive, synchronous to the magmatic evolution and associated to the crystallization of the main minerals. On these bases, we can exclude mixing of different parental magmas as the primary process responsible for the selective enrichments documented in the gabbros from the Tihama Asir igneous complex.

#### *6.2.4. Reactive crystallization*

*Reactive crystallization* i.e., assimilation of mineral matrix and synchronous fractional crystallization at decreasing temperatures (Collier & Kelemen, 2010), has been extensively invoked to explain textural observations (e.g., dissolution microstructures) and trace element enrichments in the continental (e.g., De Paolo, 1981; Bohrson & Spera, 2001; Andrews *et al.*, 2008; Antonicelli *et al.*, 2020) and oceanic lithosphere (e.g., Kelemen *et al.*, 1995; Lissenberg & Dick, 2008; Lissenberg *et al.*, 2013; Leuthold *et al.*, 2018; Basch, 2018; Basch *et al.*, 2019a; Ferrando *et al.*, 2021b). The assimilation of a pre-existing mineral matrix is driven by chemical disequilibrium between the intruding melt and the host rock and causes the modification and hybridization of the melt composition (e.g., De Paolo, 1981; Natland & Dick, 2002; France *et al.*, 2009; Koepke *et al.*, 2011; Leuthold *et al.*, 2014; Sparks *et al.*,

2019; Antonicelli *et al.*, 2020). This modification in melt composition can in turn lead to the anticipation and/or saturation of mineral phases not expected from the fractional crystallization of the primary melt composition (e.g., Dick & Natland, 1996; Collier & Kelemen, 2010; Sanfilippo *et al.*, 2016; Basch *et al.*, 2019b; Brunelli *et al.*, 2020).

Consistently, the oxide gabbro from the Tihama Asir contains discrete quantities of interstitial phlogopite (4 vol%; Fig. 3e). In oceanic settings, dark mica has only been documented as an accessory phase in felsic veins formed from extremely fractionated MORB melts (e.g., Nguyen *et al.*, 2018). The crystallization of substantial quantities of such a potassium-rich mineral is not predicted upon simple fractional crystallization of MORB-type melts (e.g., Botcharnikov *et al.*, 2008; Koepke *et al.*, 2018), but rather requires addition of K-rich material. On the same line of evidence, bulk-rock enrichments in Rb, Ba, Th, U and LREE require the assimilation of material with crustal affinity. Given that the Tihama Asir gabbros are in primary contact with the Arabian continental crust, we argue that continental material from the extended Arabian margin was assimilated into the crystal mush during the formation of the gabbroic intrusion.

To assess whether assimilation of continental crust and hybridization of a MORB-type melt can explain the composition of the Tihama Asir gabbros, we opted for a model of Assimilation-Fractional Crystallization process (AFC) using the equation of De Paolo (1981), originally designed to compute the geochemical impact of processes of crustal assimilation. Considering that our aim is to mathematically reproduce the analyzed enrichments in highly incompatible elements during a well-constrained petrological process, we preferred this simple approach to more realistic and complex geochemical and thermodynamic models available in literature (e.g., Magma Chamber Simulator, see Bohrson *et al.*, 2014, 2020; Heinonen *et al.*, 2020).

### 6.3. Continental crust assimilation: geochemical modeling

Our geochemical model is designed to reproduce the enrichments in highly incompatible elements within the minerals of the Tihama Asir gabbros. To do so, we first computed the melts in equilibrium with clinopyroxene cores and rims, using the cpx/melt partition coefficients from the compilation by Basch *et al.*, (2018). Equilibrium melts are given in Supplementary Table S7 and are plotted in Figure 10a, b.

The computed equilibrium melt compositions show a large range of trace element absolute concentrations, with lower REE concentrations in the melts that formed the clinopyroxene

cores ($Yb_N$ = 19.6-75.1 times CI) with respect to the melts that formed the clinopyroxene rims ($Yb_N$ = 23.5-96.0 times CI), regardless of the lithology considered. Melts in equilibrium with clinopyroxene cores also show lower LREE/HREE fractionation ($La_N/Y_N$ = 1.42-4.35) than melts in equilibrium with clinopyroxene rims ($La_N/Y_N$ = 2.07-5.17). All computed melts show negative Eu, Sr and Ti anomalies (Fig. 10b), consistent with the fractionation of plagioclase and Fe-Ti oxides upon progressive crystallization of oxide-bearing gabbros (Dick *et al.*, 2000; Botcharnikov *et al.*, 2008). The enriched character of highly incompatible elements (e.g., Rb, Ba, Th, U, Zr, Hf; Fig. 10b) and the positive LREE/HREE fractionation characterizing the melts in equilibrium with the Tihama Asir clinopyroxenes from the evolved gabbroic samples do not fit with the Mid-Atlantic ridge basalts compositional field and support the involvement of crustal assimilation and hybridization of the parental MORB-type melts towards granitic compositions (see Coleman & McGuire, 1986).

To quantify the modification of the parental melt composition during progressive assimilation of continental crust, we perform an Assimilation-Fractional Crystallization (AFC) model (De Paolo, 1981). To account for the variability of tholeiitic melt compositions in the Red Sea setting and in correspondence with the nearby Afar plume (e.g., van der Zwan *et al.*, 2015), we compute AFC models using different starting melts, namely N-MORB and E-MORB compositions (after Sun & McDonough, 1989). Additionally, we performed an AFC model using the composition of a basaltic dike crosscutting the layered gabbro unit (TA01-Tlg1b; Table 1) as starting melt. This basaltic dike shows trace element compositions ($La_N/Sm_N$ = 1.08) similar to E-MORB melts. Given the structural relationships with the gabbroic body and the difference with the Quaternary basalts outcropping nearby, we infer that this dike likely formed soon after the solidification of the gabbros and may thereby be representative of the parental melt composition of the igneous complex. Our AFC models simulate the assimilation of two different crustal components, namely the average Upper Continental Crust (UCC) and the average Lower Continental Crust (LCC) as estimated by McLennan (2001). In these AFC models, we simulate the progressive crystallization of a MORB-type melt at decreasing melt mass; accordingly, we computed the process of reactive crystallization assuming progressive changes in the saturated phases at decreasing melt mass. We modelled the crystallization of a primitive olivine gabbro (ol:pl:cpx = 20:50:30 vol%) from F = 1 (100% melt mass) to F = 0.8, followed by the crystallization of a gabbro (pl:cpx = 50:50 vol%) from F = 0.8 to F = 0.4 and the crystallization of an oxide gabbro (pl:cpx:ilm = 48:47:5 vol%) from F = 0.4 to F = 0.1. The considered mass assimilated/mass crystallized (Ma/Mc) ranges from 0.1 to 0.9 and the partition coefficients are after Bédard (1994) and

Basch *et al.* (2018). Model parameters and results of the AFC models are given in Supplementary Table S8. To best visualize the progressive trace element variations, we did not represent the variation of single elemental ratios but modeled the evolution of the whole melt REE and trace element patterns.

Figure 11 shows the comparison between the Tihama Asir equilibrium melt compositions and the modeled evolution of an N-MORB melt composition during progressive fractionation and assimilation of UCC (Ma/Mc = 0.5; Fig. 11a, b) and LCC (Ma/Mc = 0.8; Fig. 11c, d) at decreasing melt mass (F decreasing from 1 to 0.1). The result of the models using the E-MORB and the crosscutting basaltic dike as starting melt composition are given in Supplementary Figure S1 and Supplementary Figure S2, respectively. In all AFC models, the residual melt composition shows a progressive increase in REE absolute concentrations and LREE/HREE fractionation upon fractionation and concomitant assimilation of crustal material (Fig. 11). This increase in REE absolute concentrations, $La_N/Sm_N$ and $La_N/Y_N$ ratios is accompanied by enrichments in highly incompatible elements (Rb, Ba, Th, U, Nb, Zr, Hf) and development of negative anomalies in Ba, Nb, Sr and Eu (Fig. 11b, d) that fit well the compositions from the Tihama Asir igneous complex.

Figure 12 shows clinopyroxene compositions modeled after the assimilation of UCC (Fig. 12a-d) and LCC (Fig. 12e-h) by a melt with N-MORB starting compositions, at different assimilation rates ($0.1 < Ma/Mc < 0.9$). Notably, the model successfully reproduces the change in compositions of the studied samples even if an E-MORB or the crosscutting basaltic dike are used as starting melt compositions (Supplementary Figure S3 and Supplementary Figure S4, respectively). However, using an E-MORB as starting composition, the AFC model yields initial $La_N/Sm_N$ and $Th_N/Y_N$ ratios slightly higher than the clinopyroxenes analysed in the olivine gabbros (Fig. S3, Fig. S4). Hence, although we cannot exclude that the mantle asthenosphere was somehow polluted by material deriving from the Afar plume (van der Zwan *et al.*, 2015), the parental melts of the Tihama Asir gabbros had a MORB-like trace element signature (Fig. 12). More importantly, our AFC model demonstrates that high rates of continental crust assimilation are required (Ma/Mc = 0.3-0.6 for UCC assimilation, Ma/Mc = 0.6-0.9 for LCC assimilation) to reproduce the Tihama Asir gabbro absolute concentrations ($La_N$; Fig. 12a, e) and REE fractionation ($La_N/Y_N$, Fig. 12b, f; $La_N/Sm_N$, Fig. 12c, g; $Th_N/Y_N$; Fig. 12d, h). The higher assimilation rates required while considering LCC assimilation result from lower trace element absolute concentrations within the assimilated continental material (see inserts in Fig. 11).

In summary, our models suggest that the process of continental crust assimilation previously inferred by Coleman & McGuire (1986) and McGuire & Coleman (1986) successfully reproduces the large geochemical variability of the different lithologies forming the Tihama Asir gabbros. The modeled hybridization process involves progressive crystallization of a MORB-type melt during concomitant assimilation of the host continental crust at relatively elevated assimilation rates (Ma/Mc = 0.3-0.9; Fig. 12; Fig. S3; Fig. S4). The modeled enrichments in LREE and highly incompatible elements cover the whole range of compositions reported in the Tihama Asir olivine gabbros, cpx-gabbros and oxide gabbro (Fig. 11, Fig. 12; Fig. S1; Fig. S2; Fig. S3; Fig. S4). Assimilation of either UCC or LCC allows us to reproduce the compositions of the Tihama Asir gabbros; discerning the assimilated portion of continental crust requires detailed isotopic analyses of the Tihama Asir gabbros and is beyond the scope of this study. A detailed quantification of the continental crust assimilation process will be provided in a separate study.

### 6.4. Extraction of hybridized melts and formation of basalt dike swarms

The Tihama Asir gabbroic bodies are associated with coeval basaltic intrusions (20-24 Ma; e.g., Stern & Johnson, 2019), forming crosscutting dikes and dike swarms that increase in density from the east to the west, towards the Red Sea. These dikes are characterized by decimetre- to metre-size thickness (Fig. 2c, d) and chilled margins at the contact with their host gabbroic and continental rocks. These chilled margins are indicative of fast cooling and thus emplacement of the intrusion into a cold environment (e.g., Huppert & Sparks, 1989; Hayman *et al.*, 2009). Figure 13 shows the bulk-rock REE composition of the Tihama Asir basalts (see also Supplementary Table S1). We distinguish two families of dikes on the basis of their field relationships and major and trace element compositions: *i)* the Jabal Sawdah dike swarm intruded into continental basement and, *ii)* the Masliyah basalts crosscutting the layered gabbros.

The Jabal Sawdah basalts show a large range of major and trace element compositions and show enrichments in the most incompatible elements with respect to the HREE (Fig. 4e, f, g, h). The LREE-enriched patterns of the basalts are similar to the melts computed in equilibrium with clinopyroxene cores in the Tihama Asir gabbros, both in terms of absolute concentrations and LREE/HREE fractionation (Fig. 13). Therefore, we infer that the melts that intruded the continental basement and formed the dike swarm presented the same hybridized character as the melts forming the most evolved gabbros. This implies that hybrid

melts were extracted from the uppermost portions of the gabbroic crystal mush (e.g., Coogan & Dosso, 2016). Moreover, our AFC models demonstrate that most of the Tihama Asir clinopyroxene compositions require high assimilation rates, but with a remaining melt mass of at least 30% (indicated as F > 0.3 in Fig. 11c, d; Fig. 12). This suggests that the initial process of reactive crystallization occurred within a crustal magma chamber, followed by the extraction of the hybridized melt to form the overlying dike swarm (Fig. 14).

Notably, the Jabal Sawdah basalts show bulk-rock REE compositions similar to the melt in equilibrium with the clinopyroxene cores, instead of the clinopyroxene rims (Fig. 13). This suggests that melt extraction occurred prior to the crystallization of the late-stage melts forming the clinopyroxene rims. The extraction from the gabbroic crystal mush was likely relatively scarce, since the presence of poikilitic clinopyroxenes and oxides, associated with interstitial amphibole (Fig. 3b, c) and millimetre-size gabbronoritic aggregates (Fig. 3d) are evidence of late-stage crystallization during closure of the magmatic system (i.e., after partial extraction; Lissenberg & Dick, 2008; Leuthold *et al.*, 2018). Microstructural evidence consistent with our scenario of partial melt extraction from a gabbroic crystal mush can be found in the Tihama Asir olivine- and cpx-gabbros. Indeed, elongated plagioclase crystals form weak foliations and show diffuse occurrence of bending and mechanical twins (Fig. 3b, c). These characteristics have been reported in microstructural studies of crystal mush compaction (Meurer & Boudreau, 1998; Namur *et al.*, 2015; Cheadle & Gee, 2017; Bertolett *et al.*, 2019; Ferrando *et al.*, 2021a), in which the latter process leads to deformation and physical reorganization of the crystals according to their morphology. Therefore, based on combined microstructural and geochemical evidence in the Tihama Asir gabbros and dike swarm, we infer that after partial reactive crystallization of the gabbroic bodies, the hybridized melt was in part extracted from the gabbroic crystal mush and intruded into cold continental crust to ultimately form dike swarms presenting chilled margins, similar to the Jabal Sawdah basalts (Fig. 14). The interstitial melt that remained in the compacted crystal mush then crystallized poikilitic clinopyroxenes and gabbronoritic aggregates during late-stage crystallization at decreasing temperature (e.g., Meurer & Boudreau, 1998; Namur *et al.*, 2015; Ferrando *et al.*, 2021b).

Conversely to the Jabal Sawdah dike swarm, the dikes crosscutting the Masliyah layered gabbro show relatively flat REE patterns ($La_N/Y_N$ = 1.05-1.26; Fig. 13; Supplementary Table S1). The latter suggest little or no continental crust assimilation and hybridization (Fig. 11a, b; Fig. 12). Given that assimilation of the host rock occurs mainly within magma chambers and crystal mushes (e.g., Coogan & Dosso, 2016), we infer that the crosscutting basalts

experienced rapid extraction from deep magma chambers towards colder levels through an already cooled gabbroic body, thus allowing for brittle fracturing and for the formation of chilled margins.

### 6.5. Implications on the geodynamic evolution of the Red Sea rift system

The western Arabian plate exposes a Cenozoic volcanic province formed during the emplacement of the Afar plume and lithospheric thinning related to the Red Sea rifting (e.g., Bosworth & Stockli, 2016; Sanfilippo *et al.*, 2019; Stern & Johnson, 2019). Yet, it remains unclear if the syn-rift magmatism influenced the rift-to-drift transition and breakup of the Arabian-Nubian Shield (ANS) (e.g., Bialas *et al.*, 2010; Ligi *et al.*, 2015; Stern & Johnson, 2019). Based on the abundant Cenozoic volcanism along the Arabian margin, Stern & Johnson (2019) recently proposed to define the Red Sea as a volcanic rifted margin. Volcanic rifted margins, of which the Greenland-Norway margins are the prime examples (e.g., Hopper *et al.*, 2003; Voss & Jokat 2007; Franke, 2013), are characterized by extensive syn-rift magmatism leading to the formation of seaward dipping reflectors, considered evidence of a rapid transition from rifting to oceanic spreading (e.g., Bialas et al., 2010). In the same line of evidence, the rifting and break-up of the South China Sea has recently been re-evaluated based on seismic data and IODP sampling of MORB-type pillow basalts in the distal margin (IODP Expedition 367/368; Larsen *et al.*, 2018 and references within). There, fast rift-to-drift transition is thought to have been induced by strong and focused syn-rift magmatism that accompanied lithospheric thermal weakening and thinning.

Although the opening of the Red Sea was accompanied by numerous intrusions within the rifted ANS (Keranen *et al.*, 2004; Kendall *et al.*, 2005) and is considered a volcanic rifted margin, most studies concur that the rifting phase was protracted over at least ~7 Ma (e.g., Amalki *et al.*, 2015; Ligi *et al.*, 2015; Augustin *et al.*, 2021). Conversely to the focused magmatism documented in the Greenland-Norway and South China Sea margins, it appears that the magmatism in the Red Sea rift system did not allow for immediate continental break-up and led to a long-lived rifting process of the ANS, before the localization of magmatism and deformation drove continental breakup and onset of oceanic spreading delayed of at least ~7 Ma (El Khrepy *et al.*, 2021).

In the studied area, the Tihama Asir igneous complex is closely associated to numerous basaltic dikes intruded within the continental crust and formed as part of the extensive magmatism associated with the initial Red Sea rifting phase (~24.3-20.0 Ma; Bosworth &

Stockli, 2016). Our study documents that the emplacement of MORB-type gabbroic plutons was accompanied by extensive assimilation of the host continental crust (Fig. 11; Fig. 12), and that the melt hybridized within the gabbroic crystal mush was extracted and formed dike swarms intruded within the upper continental crust (Fig. 13; Fig. 14). The formation of the Tihama Asir therefore fits well into the context of volcanic rifted margins, in which the thinned continental crust is intruded and partially replaced by hybridized oceanic crust. Notably, as it is documented in natural settings and modeled numerically, the addition of mafic material into rifted margins can have contrasting effects on rifting and break-up processes, namely: *i)* focused magmatism can lead to rapid continental break-up and onset of seafloor spreading (e.g., Bialas *et al.*, 2010; Larsen *et al.*, 2018), *ii)* magma-compensated crustal thinning, although involving sustained magmatism, prevents continental break-up (e.g., Thybo & Nielsen, 2009; Bastow & Keir, 2011; Chenin *et al.*, 2019), and *iii)* the widening of the deformed zone, with extensive but diffuse melt addition within the rifted continental crust, leads to a delay in continental rupture (e.g., El Khrepy *et al.*, 2021). Given that the Red Sea rifting was protracted over more than 7 Ma, we suggest that the two latter hypotheses are more likely to have driven the tectonic evolution of the Red Sea rift system and emphasize that the timing and distribution of magmatism during extension are critical factors in the development of a rift system.

## 7. CONCLUSIONS

The Tihama Asir igneous complex formed as part of the extensive magmatism that occurred during the early phase of the Red Sea continental rifting (25-20 Ma). It represents a key location to study the initial phase of syn-rift magmatism and its influence on the geodynamic evolution of the Red Sea rift system. The Tihama Asir plutons are composed of gabbros ranging in composition from MORB-type olivine gabbros to oxide gabbros showing the discrete occurrence of dark mica and enrichments in highly incompatible trace elements (e.g., Rb, Ba, Th, U, Sr, LREE). The modal, bulk and mineral compositions of the gabbroic bodies indicate that a process of progressive crustal assimilation during concomitant crystallization drove the chemical evolution of the MORB-type gabbroic crystal mush. The melts hybridized by crustal contamination were subsequently extracted and intruded into the Arabian Shield continental crust, forming the dike swarms exposed along the western Arabian margin. Our results confirm that syn-rift magmatism led to the partial replacement of the thinned

continental crust by MORB-type gabbroic bodies, in turn suggesting that oceanic magmatism started prior to continental break-up. Extensive syn-rift magmatism is consistent with the interpretation of the Red Sea rift system as a volcanic rifted margin, in which the extensive but diffuse syn-rift magmatism possibly hampered continental break-up and led to the protracted rifting documented for the Red Sea system.

**Acknowledgements**

We thank V. Troll for his work as editor and the two anonymous reviewers and F.M. van der Zwan for their constructive comments that helped us improve the quality of the manuscript. This work is the result of a joint effort of the Saudi Geological Survey (SGS), and the Istituto di Scienze Marine, CNR of Bologna (ISMAR-CNR). We thank Captain P. Dimala and helicopter assistants Abdulhadi and A.Al-Harbi for their collaboration during the fieldwork. We thank Dr. Z.A. Nawab, former SGS President and Dr. A.M. Alattas, former SGS Assistant President for Technical Affairs. We would also like to extend our thanks to the Assistant President, Technical Affairs, Mr. Saleh A. Sefry for his cooperation and support in publishing this research. Colleagues at the Center for Marine Geology (CMG-SGS) are also thanked for their participation and assistance in the numerous field expeditions. The work was supported by the SGS. Matteo Deraco is kindly thanked for a preliminary petrographic and geochemical characterization. The work was supported by the PRIN2017 Programme (PRIN_2017KY5ZX8).

## References

Abu El-Rus, M.M.A. & Rooney, A.O. (2017). Insights into the lithosphere to asthenosphere melting transition in northeast Africa: evidence from the Tertiary volcanism in middle Egypt. *Chemical Geology* **455**, 282-303.

Almalki, K.A., Betts, P.G., & Ailleres, L. (2015). The Red Sea - 50 years of geological and geophysical research. *Earth Science Reviews* **147**, 109–140, doi: 10.1016/j.earscirev.2015.05.002.

Anderson, A.T. (1976). Magma mixing - petrological process and volcanological tool. Journal of Volcanology and Geothermal Research **1**, 3–33, doi: 10.1016/0377-0273(76)90016-0

Andrews, B.J., Gardner, J.E., Housh, T.B. (2008). Repeated recharge, assimilation, and hybridization in magmas erupted from El Chichon as recorded by plagioclase and

amphibole phenocrysts. *Journal of Volcanology and Geothermal Research* **175**, 415–426 doi: 10.1016/j.jvolgeores.2008.02.017.

Antonicelli, M., Tribuzio, R., Liu, T. & Wu, F.-Y. (2020). Contaminating melt flow in magmatic peridotites from the lower continental crust (Rocca d'Argimonia sequence, Ivrea–Verbano Zone). *European Journal of Mineralogy*, **32**, 587–612, doi: 10.5194/ejm-32-587-2020.

Audin, L., Quidelleur, X., Coulié, E., Courtillot, V., Gilder, S., Manighetti, I., Gillot, P.-Y., Tapponnier, P. & Kidane, T. (2004). Paleomagnetism and K-Ar and $^{40}Ar/^{39}Ar$ ages in the Ali Sabieh area (Republic of Djibouti and Ethiopia): constraints on the mechanism of Aden ridge propagation into southeastern Afar during the last 10 Myr. *Geophysical Journal International* **158**, 327–345.

Augustin, N., Devey, C. W., van der Zwan, F. M., Feldens, P., Tominaga, M., Bantan, R. A. & Kwasnitschka, T. (2014). The rifting to spreading transition in the Red Sea. *Earth and Planetary Science Letters* **395**, 217-230, doi: 10.1016/j.epsl.2014.03.047.

Augustin, N., van der Zwan, F. M., Devey, C. W. & Brandsdòttir, B. (2021). 13 million years of seafloor spreading throughout the Red Sea Basin. *Nature Communications* **12**, 2427, doi: 10.1038/s41467-021-22586-2.

Barberi, F., Borsi, S., Ferrara, G., Marinelli, G., Santacroce, R., Tazieff, H. & Varet, J. (1972). Evolution of the Danakil Depression (Afar, Ethiopia) in light of radiometric age determinations. *Journal of Geology* **80**, 720–729.

Barberi, F., Santacroce, R. & Varet, J. (1975). Structural evolution of the Afar triple junction. In: *Pilger, A., Rösler, A. (Eds.) Afar depression of Ethiopia, Proceedings of an international symposium on the afar region and related rift problems*, vol **1**. Bad Bergzabern FR, Germany, 1–6 April 1974. E. Schweizerbartsche Verlagsbuchhandlung, Stuttgart, pp. 38–54.

Basch, V. (2018). Melt–rock interactions in the oceanic lithosphere: microstructural and petro-geochemical constraints from ophiolites. *PhD thesis, Università degli Studi di Genova*, doi: 10.15167/basch-valentin_phd2018-05-10.

Basch, V., Rampone, E., Crispini, L., Ferrando, C., Ildefonse, B. & Godard, M. (2018). From mantle peridotites to hybrid troctolites: textural and chemical evolution during melt–rock interaction history (Mt. Maggiore, Corsica, France). *Lithos* **323**, 4-23, doi: 10.1016/j.lithos.2018.02.025.

Basch, V., Rampone, E., Crispini, L., Ferrando, C., Ildefonse, B. & Godard, M. (2019a). Multi-stage Reactive Formation of Troctolites in Slow-spreading Oceanic Lithosphere (Erro-Tobbio, Italy): a Combined Field and Petrogeochemical Study. *Journal of Petrology* **60**, 873-906, doi: 10.1093/petrology/egz019.

Basch, V., Rampone, E., Borghini, G., Ferrando, C. & Zanetti, A. (2019b). Origin of pyroxenites in the oceanic mantle and their implications on the reactive percolation of

depleted melts. *Contributions to Mineralogy and Petrology* **174**, 97, doi: 10.1007/s00410-019-1640-0.

Bastow, I.D. & Keir, D. (2011). The protracted development of the continent-ocean transition in Afar. *Nature Geoscience*, **4**, 248-250, doi: 10.1038/ngeo1095.

Bédard, J. H. (1994). A procedure for calculating the equilibrium distribution of trace elements among the minerals of cumulate rocks, and the concentration of trace elements in the coexisting liquids. *Chemical Geology* **118**, 143-153.

Bellahsen, N., Faccenna, C., Funiciello, F., Daniel, J. M., & Jolivet, L. (2003). Why did Arabia separate from Africa? Insights from 3-D laboratory experiments. *Earth and Planetary Science Letters* **216** (3), 365–381.

Bertolett, E.M., Prior, D.J., Gravley, D.M., Hampton, S.J. & Kennedy, B.M. (2019). Compacted cumulates revealed by electron backscatter diffraction analysis of plutonic lithics. *Geology* **47**, 445-448, doi: 10.1130/G45616.1.

Bialas, R.W., Buck, W.R. & Qin, R. (2010). How much magma is required to rift a continent? *Earth and Planetary Science Letters* **292**, 68–78.

Blank, H.R., & Gettings, M.E. (1984). Reconnaissance geologic map of the Jizan quadrangle, sheet 16/42B. *Ministry of Petroleum and Mineral Resources, Kingdom of Saudi Arabia.*

Bohannon, R.G. (1986). Tectonic configuration of the western Arabian continental margin, Southern Red Sea. *Tectonics* **5**, 477-499.

Bohrson, W.A. & Spera, F.J. (2001). Energy-constrained open-system magmatic processes II: Application of Energy-Constrained Assimilation-Fractional Crystallization (EC-AFC) model to magmatic systems. *Journal of Petrology* **42**, 1019-1041.

Bohrson, W.A., Spera, F.J., Ghiorso, M.S., Brown, G.A., Creamer, J.B. & Mayfield, A. (2014). Thermodynamic model for energy-constrained open system evolution of crustal magma bodies undergoing simultaneous recharge, assimilation and crystallization: the magma chamber simulator. *Journal of Petrology* **55**, 1685–1717, doi: 10.1093/petrology/egu036.

Bohrson, W.A., Spera, F.J., Heinonen, J.S., Brown, G.A., Scruggs, M.A., Adams, J.V., Takach, M.K., Zeff, G. & Suikkanen, E. (2020). Diagnosing open-system magmatic processes using the Magma Chamber Simulator (MCS): part I-major elements and phase equilibria. *Contributions to Mineralogy and Petrology* **175**, 104, doi: 10.1007/s00410-020-01722-z.

Bonatti, E. (1985). Punctiform initiation of seafloor spreading in the Red Sea during transition from continental to an oceanic rift. *Nature* **316**, 33-37.

Bonatti, E. & Seyler, M. (1987). Crustal underplating and evolution in the Red Sea rift. *Journal of Geophysical Research* **92**, 12083–12821, doi: 10.1029/JB092iB12p12803.

Bonatti, E., Cipriani, A. & Lupi, L. (2015). The Red Sea: birth of an ocean. In: *Rasul, N.M.A., Stewart, I.C.F. (Eds.) The Red Sea: the formation, morphology, oceanography, and environment of a young ocean basin*. Springer Earth System Sciences, Berlin Heidelberg, 29–44, doi: 10.1007/978-3-662-45201-1_2.

Bosworth, W., Huchon, P. & McClay, K. (2005). The Red Sea and Gulf of Aden Basins. In: *Catuneanu, O., Guiraud, R., Eriksson, P. Thomas, B., Shone, R. and Key, R. (Eds.) Phanerozoic Evolution of Africa. Journal of African Earth Sciences*, **43**: 334–378, doi: 10.1016/j.jafrearsci.2005.07.020.

Bosworth, W. (2015). Geological Evolution of the Red Sea: Historical Background, Review and Synthesis. In: *Rasul, N.M. and Stewart, I.C.F. (Eds.) The Red Sea: Its Origin, Structure and Environment*. Springer Earth System Sciences, Berlin Heidelberg, 45–78.

Bosworth, W. & Stockli, D.F. (2016). Early magmatism in the greater Red Sea rift: timing and significance. *Canadian Journal of Earth Sciences* **53**, 1158-1176, doi: 10.1139/cjes-2016-0019.

Bosworth, W., Khalil, S.M., Ligi, M., Stockli, D.F. & McClay, K.R. (2020). Geology of Egypt: The Northern Red Sea. In: *Hamimi, Z., El-Barkooky, A., Martínez Frías, J., Fritz, H., Abd El-Rahman, Y. (Eds.) The Geology of Egypt*, Regional Geology Reviews Series, Springer-Verlag Berlin, 343-374, doi: 10.1007/978-3-030-15265-9_9.

Botcharnikov, R.E., Almeev, R., Koepke, J. & Holtz, F. (2008). Phase relations and liquid lines of descent in hydrous ferrobasalt - Implications for the Skaergaard Intrusion and Columbia River Flood Basalts. *Journal of Petrology* 49: 1687-1727.

Brunelli, D., Sanfilippo, A., Bonatti, E., Skolotnev, S., Escartin, J., Ligi, M., Ballabio, G. & Cipriani, A. (2020). Origin of oceanic ferrodiorites by injection of nelsonitic melts in gabbros at the Vema Lithospheric Section, Mid Atlantic Ridge. *Lithos* **368-369**, 105589, doi: 10.1016/j.lithos.2020.105589.

Burke, K., & Dewey, J.F. (1973). Plume-generated triple junctions: key indicators in applying plate tectonics to old rocks. *Journal of Geology* **81**, 406–433, doi:10.1086/627882.

Burke, K. (1996). The African plate. *South African Journal of Geology* **99**, 341-409.

Cashman, K.V., Sparks, R.S. & Blundy, J.D. (2017). Vertically extensive and unstable magmatic systems: A unified view of igneous processes. *Science* **355**, 1280, doi: 10.1126/science.aag3055.

Chazot, G., Menzies, M.A., & Baker, J. (1998). Pre-, syn- and post-rift volcanism on the southwestern margin of the Arabian plate. In: *Purser, B.H. and Bosence, D.W.J. (Eds.) Sedimentation and Tectonics of Rift Basins: Red Sea–Gulf of Aden*. Chapman and Hall, London. 50–55.

Cheadle, M.J. & Gee, J.S. (2017). Quantitative textural insights into the formation of gabbro in mafic intrusions. *Elements* **13**, 409-414, doi: 10.2138/gselements.13.6.409.

Chenin, P., Jammes, S., Lavier, L., Manatschal, G., Picazo, S., Muntener, O., Karner, G.D., Figueredo, P.H. & Johnson, C. (2019). Impact of mafic underplating and mantle depletion on subsequent rifting: a numerical modeling study. *Tectonics,* **38**, 2185-2207, doi: 10.1029/2018TC005318.

Cochran, J.R. (1983). A model for development of the Red Sea. *Bulletin of the American Association of Petroleum Geologists* **67**, 41-69, doi: 10.7916/d8-kftb-n555.

Cochran, J.R. (2005). Northern Red Sea: Nucleation of an oceanic spreading center within a continental rift. *Geochemistry, Geophysics, Geosystems* **6**, Q03006, doi: 10.1029/2004GC000826.

Coleman, R.G., Brown, G.F. & Keith, T.E.C. (1972). Layered gabbros in southwest Saudi Arabia. *U.S. Geological Survey Professional Paper* 800-D, D143-D150.

Coleman, R.G., Blank, H.R., Jr., Hadley, D.G. & Fleck, R.G. (1975). A Miocene ophiolite on the Red Sea Coastal plain. *American Geophysical Union Transactions* **56**, 1080.

Coleman, R.G., Hadley, D.G., Fleck, R.J., Hedge, C.E. & Donato, M.M. (1979). Miocene Tihama Asir complex and its bearing on the opening of the Red Sea. In: *Al-Shanti, A.M. (Ed.) Evolution and Mineralization of the Arabian-Nubian Shield*, Vol. **1**, Oxford, Pergamon Press, Ltd. p.173-186.

Coleman, R.G. (1984). The Tihama Asir igneous complex, a passive margin ophiolite. *Proceedings of the 27th International Geological Congress, Moscow* **23**, 221-239.

Coleman, R.G. & McGuire, A.V. (1986). Magma systems related to the Red Sea opening. *Tectonophysics* **150**, 77-100.

Collier, M.L. & Kelemen, P.B. (2010). The Case for Reactive Crystallization at Mid-Ocean Ridges. *Journal of Petrology* **51**, 1913-1940, doi: 10.1093/petrology/egq043.

Coogan, L.A., Kempton, P.D., Saunders, A.D. & Norry, M.J. (2000). Melt aggregation within the crust beneath the Mid-Atlantic Ridge: evidence from plagioclase and clinopyroxene major and trace element compositions. *Earth and Planetary Science Letters* **176**, 245-257.

Coogan, L.A., Wilson, R.N., Gillis, K.M. & MacLeod, C.J. (2001). Near-solidus evolution of oceanic gabbros: insights from amphibole geochemistry. *Geochimica et Cosmochimica Acta* **65**(23), 4339-4357.

Coogan, L.A & O'Hara, M.J. (2015). MORB differentiation: *In situ* crystallization in replenished-tapped magma chambers. *Geochimica et Cosmochimica Acta* **158**, 147-161, doi: 10.1016/j.gca.2015.03.010.

Coogan, L.A. & Dosso, S.E. (2016). Quantifying Parental MORB Trace Element Compositions from the Eruptive Products of Realistic Magma Chambers: Parental EPR MORB are Depleted. *Journal of Petrology* **57**, 2105-2126, doi: 10.1093/petrology/egw059.

Cortesogno, L., Gaggero, L. & Zanetti, A. (2000). Rare earth and trace elements in igneous and high-temperature metamorphic minerals of oceanic gabbros (MARK area, Mid-Atlantic Ridge). *Contributions to Mineralogy and Petrology* **139**, 373-393, doi: 10.1007/s004100000147.

Courtillot, V. (1982). Propagating rifts and continental breakup. *Tectonics* **1**, 239–250, doi: 10.1029/TC001i003p00239.

DeMets, C. & Merkouriev, S. (2016). High-resolution estimates of Nubia-Somalia plate motion since 20 Ma from reconstructions of the Southwest Indian Ridge, Red Sea and Gulf of Aden. *Geophysical Journal International* **207**, 317–332.

De Paolo, D.J. (1981). Trace elements and isotopic effects of combined wall rock assimilation and fractional crystallization. *Earth and Planetary Science Letters* **53**, 189-202.

Dick, H.J.B. & Natland, J.H. (1996). Late-stage melt evolution and transport in the shallow mantle beneath the East Pacific Rise. In: *Mével, C., Gillis, K.M., Allan, J.F., Meyer, P.S. (Eds.) Proceedings of the Ocean Drilling Program, Scientific Results* **147**, 103-134, doi:10.2973/odp.proc.sr.147.007.1996

Dick, H.J.B., Natland, J.H., Alt, J.C., Bach, W., Bideau, D., Gee, J.S., Haggas, S., Hertogen, J.G.H., Hirth, G., Holm, P.M., Ildefonse, B., Iturrino, G.J., John, B.E., Kelley, D.S., Kikawa, E., Kingdon, A., Le Roux, P.J., Maeda, J., Meyer, P.S., Miller, D.J., Naslund, H.R., Niu, Y., Robinson, P.T., Snow, J., Stephen, R.A., Trimby, P.W., Worm, H.-U. & Yoshinobu, A. (2000). A long in-situ section of the lower ocean crust: results of ODP Leg 176 drilling at the Southwest Indian Ridge. *Earth and Planetary Science Letters* **179**, 31-51.

Edmonds, M., Cashman, K.V., Holness, M. & Jackson, M. (2019). Architecture and dynamics of magma reservoirs. *Philosophical Transactions of the Royal Society A* **377**, 20180298, doi: 10.1098/rsta.2018.0298.Faccenna, C., Becker, T.W., Jolivet, L. & Keskin, M. (2013). Mantle convection in the Middle East: Reconciling Afar upwelling, Arabia indentation and Aegean trench rollback. *Earth and Planetary Science Letters* **375**, 254–269.

El Khrepy, S., Koulakov, I., Gerya, T., Al-Arifi, N., Alajmi, M.S. & Qadrouh, A.N. (2021). Transition from continental rifting to oceanic spreading in the northern Red Sea area. *Scientific Reports* **11**, 5594, doi: 10.1038/s41598-021-84952-w.

Ferrando, C., Godard, M., Ildefonse, B. & Rampone, E. (2018). Melt transport and mantle assimilation at Atlantis Massif (IODP Site U1309): constraints from geochemical modelling. *Lithos* **323**, 24-43.

Ferrando, C., Lynn, K.J., Basch, V., Ildefonse, B. & Godard, M. (2020). Retrieving timescales of oceanic crustal evolution at Oceanic Core Complexes: Insights from diffusion modelling of geochemical profiles in olivine. *Lithos* **376-377**, 105727, doi: 10.1016/j.lithos.2020.105727.

Ferrando, C., Basch, V., Ildefonse, B., Deans, J., Sanfilippo, A., Barou, F. & France, L. (2021a). Role of compaction in melt extraction and accumulation at a slow-spreading center: Microstructures of olivine gabbros from the Atlantis Bank (IODP Hole U1473A, SWIR). *Tectonophysics* **815**, 229001, doi: 10.1016/j.tecto.2021.229001.

Ferrando, C., France, L., Basch, V., Sanfilippo, A., Boulanger, M., Deloule, E. & Tribuzio, R. (2021b). Grain size variations record segregation of residual melts in slow-spreading oceanic crust (Atlantis Bank, 57°E Southwest Indian Ridge). *Journal of Geophysical Research* **126**, e2020JB020997, doi:10.1029/2020JB020997.

Fischer, L.A., Erdmann, M., France, L., Wolff, P.E., Deloule, E., Zhang, C., Godard, M. & Koepke, J. (2016). Trace element evidence for anatexis at oceanic magma chamber roofs and the role of partial melts for contamination of fresh MORB. *Lithos* **260**, 1-8, doi: 10.1016/j.lithos.2015.05.001.

Fleet, M.E. (2003). Rock-forming minerals, Vol. 3A. Sheet silicates: Micas, second edition. *Geological Society of London*.

Follmann, J., van der Zwan, F., Preine, J., Hübscher, C., Bousquet, R. & Augustin, N. (2021). Gabbro discovery in Discovery Deep: First plutonic rock samples from the Red Sea rift axis. *Frontiers in Earth Sciences*, **9**, 742815, doi: 10.3389/feart.2021.742815.

France, L., Ildefonse, B. & Koepke, L. (2009). Interactions between magma and hydrothermal system in Oman ophiolite and in IODP Hole 1256D: Fossilization of a dynamic melt lens at fast spreading ridges. *Geochemistry, Geophysics, Geosystems* **10**, Q10O19, doi: 10.1029/2009GC002652.

Franke, D. (2013). Rifting, lithosphere breakup and volcanism: comparison of magma-poor and volcanic rifted margins. *Marine and Petroleum Geology* **43**, 63–87.

Ghebreab, W. (1998). Tectonics of the Red Sea region reassessed. *Earth-Science Reviews* **45**, 1–44.

Ghiorso, M.S. & Sack, R.O. (1995). Chemical Mass Transfer in Magmatic Processes. IV. A Revised and Internally Consistent Thermodynamic Model for the Interpolation and Extrapolation of Liquid-Solid Equilibria in Magmatic Systems at Elevated Temperatures and Pressures. *Contributions to Mineralogy and Petrology* **119**, 197-212.

Gillis, K.M., Snow, J.E., Klaus, A., Abe, N., Adrião, A.B., Akizawa, N., Ceuleneer, G., Cheadle, M.J., Faak, K., Falloon, T.J., Friedman, S.A., Godard, M., Guerin, G., Harigane, Y., Horst, A.J., Hoshide, T., Ildefonse, B., Jean, M.M., John, B.E., Koepke, J., Machi, S., Maeda, J., Marks, N.E., McCaig, A.M., Meyer, R., Morris, A., Nozaka, T., Python, M., Saha, A. & Wintsch, R.P. (2014). Primitive layered gabbros from fast-spreading oceanic crust. *Nature* **505**, 204-207, doi: 10.1038/nature12778.

Girdler, R.W. & Styles, P. (1974). Two-stage Red Sea floor spreading. *Nature* **247**, 7-11.

Godard, M., Awaji, S., Hansen, H., Hellebrand, E., Brunelli, D., Johnson, K., Yamasaki, T., Maeda, J., Abratis, M., Christie, D., Kato, Y., Mariet, C. & Rosner, M. (2009).

Geochemistry of a long in-situ section of intrusive slow-spread oceanic lithosphere: Results from IODP Site U1309 (Atlantis Massif, 30°N Mid-Atlantic-Ridge). *Earth and Planetary Science Letters* **279**, 110-122.

Hall, S.A., Andreason, G.E. & Girdler, R.W. (1977). Total intensity magnetic anomaly map of the Red Sea and adjacent coastal areas, a description and preliminary interpretation, vol 22. *Saudi Arabian Directorate General Mineral Resources Bulletin, Red Sea Research* 1970-1975: F1-F15.

Hayman, N.W., Anma, R., & Veloso, E.E (2009). Data report: microstructure of chilled margins in the sheeted dike complex of IODP Hole 1256D. In: *Teagle, D.A.H., Alt, J.C., Umino, S., Miyashita, S., Banerjee, N.R., Wilson, D.S., and the Expedition 309/312 Scientists, Proceedings IODP* **309/312**: Washington, DC (Integrated Ocean Drilling Program Management International, Inc.), doi:10.2204/iodp.proc.309312.205.2009.

Hegner, E. & Pallister, J.S. (1989). Pb, Sr, and Nd isotopic characteristics of Tertiary Red Sea rift volcanics from the central Saudi Arabian coastal plain. *Journal of Geophysical Research* **94**, 7749-7755, doi: 10.1029/JB094iB06p07749.

Heinonen, J.S., Bohrson, W.A., Spera, F.J., Brown, G.A., Scruggs, M. & Adams, J. (2020). Diagnosing open-system magmatic processes using the Magma Chamber Simulator (MCS): part II—trace elements and isotopes. *Contributions to Mineralogy and Petrology* **175**, 105, doi: 10.1007/s00410-020-01718 -9

Hempton, M.R. (1987). Constraints on Arabian plate motion and extensional history of the Red Sea. *Tectonics* **6**, 687–705. doi:10.1029/TC006i006p00687.

Hopper, J.R., Dahl-Jensen, T., Holbrook, W.S., Larsen, H.C., Lizarralde, D., Korenaga, J., Kend, G.M., Kelemen, P.B. (2003). Structure of the SE Greenland margin from seismic reflection and refraction data: implications for nascent spreading center subsidence and asymmetric crustal accretion during North Atlantic opening. Journal of Geophysical Research **108**.

Hughes, G.W., Varol, O. & Beydoun, Z.R. (1991). Evidence for Middle Oligocene rifting of the Gulf of Aden and for Late Oligocene rifting of the southern Red Sea. *Marine and Petroleum Geology* **8**, 354–358.

Huppert, H.E. & Sparks, R.S.J. (1989). Chilled margins in igneous rocks. *Earth and Planetary Science Letters* 92 (3-4), 397-405, doi: 10.1016/0012-821X(89)90063-0.

Jenner F.E. & O'Neill H.St.C. (2012). Analysis of 60 elements in 616 ocean floor basaltic glasses. *Geochemistry, Geophysics, Geosystems* **13**, doi: 10.1029/2011GC004009.

Kelemen, P.B., Shimizu, N. & Salters, V.J.M. (1995). Extraction of mid-ocean-ridge basalt from the upwelling mantle by focused flow of melt in dunite channels. *Nature* **375**, 747-753.

Kendall, J.M. & Lithgow-Bertelloni, C. (2016). Why is Africa rifting? In: *Wright, T.J., Ayele, A., Ferguson, D.J., Kidane, T. and Vye-Brown, C. (Eds.) Magmatic rifting and active volcanism. Geological Society of London, Special Publications* **420**, 11–30.

Kendall, J.M., Stuart, G.W., Ebinger, C.J., Bastow, I.D., Keir, D. (2005). Magma-assisted rifting in Ethiopia. *Nature* **433**, 146-148.

Keranen, K., Klemperer, S.L., Gloaguen, R. & EAGLE Working Group (2004). Three-dimensional seismic imagining of a protoridge axis in the Main Ethiopian rift. *Geology* **32**, 949–952.

Koepke, J., France, L., Muller, T., Faure, F., Goetze, N., Dziony, W. & Ildefonse, B. (2011). Gabbros from IODP Site 1256, equatorial Pacific: Insight into axial magma chamber processes at fast spreading ocean ridges. *Geochemistry, Geophysics, Geosystems* **12**, Q09014, doi: 10.1029/2011GC003655.

Koepke, J., Botcharnikov, R.E. & Natland, J.H. (2018). Crystallization of late-stage MORB under varying water activities and redox conditions: Implications for the formation of highly evolved lavas and oxide gabbro in the ocean crust. *Lithos* **323**, 58-77, doi: 10.1016/j.lithos.2018.10.001.

Langmuir, C.H. (1989). Geochemical consequences of in situ crystallization. *Nature* **340**, 199-205, doi: 10.1038/340199a0.

Larsen, H.C., Mohn, G., Nirrengarten, M., Sun, Z., Stock, J., Jian, Z., Klaus, A., Alvarez-Zarikian, C.A., Boaga, J., Bowden, S.A., Briais, A., Chen, Y., Cukur, D., Dadd, K., Ding, W., Dorais, M., Ferré, E.C., Ferreira, F., Furusawa, A., Gewecke, A., Hinojosa, J., Höfig, T.W., Hsiung, K.H., Huang, B., Huang, E., Huang, X.L., Jiang, S., Jin, H., Johnson, B.G., Kurzawski, R.M., Lei, C., Li, B., Li, L., Li, Y., Lin, J., Liu, C., Liu, C., Liu, Z., Luna, A.J., Lupi, C., McCarthy, A., Ningthoujam, L., Osono, N., Peate, D.W., Persaud, P., Qiu, N., Robinson, C., Satolli, S., Sauermilch, I., Schindlbeck, J.C., Skinner, S., Straub, S., Su, X., Su, C., Tian, L., van der Zwan, F.M., Wan, S., Wu, H., Xiang, R., Yadav, R, Yi, L., Yu, P.S., Zhang, C., Zhang, J., Zhang, Y., Zhao, N., Zhong, G. & Zhong, L. (2018). Rapid transition from continental breakup to igneous oceanic crust in the South China Sea. *Nature Geosciences* **11**, 782-789, doi: 10.1038/s41561-018-0198-1.

Lazar, M., Ben-Avraham, Z. & Garfunkel, Z. (2012). The Red Sea - new insights from recent geophysical studies and the connection to the Dead Sea fault. *Journal of African Earth Sciences* **68**, 96–110.

Leake, B.E., Woolley, A.R., Arps, C.E.S., Birch, W.D., Gilbert, M.C., Grice, J.D., Hawthorne, F.C., Kato, A., Kisch, H.J., Krivovichev, V.G., Linthout, K., Laird, J., Mandarino, J., Maresch, W.V., Nickel, E.H., Schumaker, J.C., Smith, D.C., Stephenson, N.C.N., Ungaretti, L., Whittaker, E.J.W. & Youzhi, G. (1997). Nomenclature of amphiboles: report of the subcommittee on amphiboles of the International Mineralogical Association Commission on New Minerals and Mineral Names. *The Canadian Mineralogist* **35**, 219-246.

Leroy, S., Gente, P., Fournier, M., d'Acremont, E., Patriat, P., Beslier, M.-O., Bellahsen, N., Maia, M., Blais, A., Perrot, J., Al-Kathiri, A., Merkouriev, S., Fleury, J.-M., Ruellan, P.-Y., Lepvrier, C. & Huchon, P. (2004). From rifting to spreading in the eastern Gulf of Aden: a geophysical survey of a young oceanic basin from margin to margin. *Terra Nova* **16**, 185-192.

Leuthold, J., Blundy, J.D., Holness, M.B. & Sides, R. (2014). Successive episodes of reactive liquid flow through a layered intrusion (Unit 9, Rum Eastern Layered Intrusion, Scotland). *Contributions to Mineralogy and Petrology*, **168**, 1021, doi: 10.1007/s00410-014-1021-7.

Leuthold, J., Lissenberg, C.J., O'Driscoll, B., Karakas, I., Falloon, T., Klimentyeva, D.N. & Ulmer, P. (2018). Partial melting of lower oceanic crust gabbro: Constraints from poikilitic clinopyroxene primocrysts. *Frontiers in Earth Science* **6**, 15, doi: 10.3389/feart.2018.00015.

Levi, S. & Riddihough, R. (1986). Why are marine magnetic anomalies suppressed over sedimented spreading centers? *Geology* **14**, 651–654.

Ligi, M., Bonatti, E., Bortoluzzi, G., Cipriani, A., Cocchi, L., Caratori Tontini, F., Carminati, E., Ottolini, L. & Schettino, A. (2012). Birth of an ocean in the Red Sea: Initial pangs. *Geochemistry, Geophysics, Geosystems* **13** (8), doi: 10.1029/2012GC004155.

Ligi, M., Bonatti, E. & Rasul, N.M.A. (2015). Seafloor spreading initiation: geophysical and geochemical constraints from the Thetis and Nereus deeps, central Red Sea. In: *Rasul NMA, Stewart ICF (eds.) The Red Sea: the formation, morphology, oceanography and environment of a young ocean basin. Springer Earth System Sciences, Berlin*, 79-98, doi: 10.1007/978-3-662-45201-1_4.Ligi, M., Bonatti, E., Bosworth, W., Cai, Y., Cipriani, A., Palmiotto, C., Ronca, S. & Seyler, M. (2018). Birth of an ocean in the Red Sea: Oceanic-type basaltic melt intrusions precede continental rupture. *Gondwana Research* **54**, 150-160, doi: 10.1016/j.gr.2017.11.002.

Ligi, M., Bonatti, E., Bosworth, W. & Ronca, S. (2019). Oceanization starts at depth during continental rupturing in the northern Red Sea. In: *Rasul, N.M.A. and Stewart, I.C.F. (Eds.) Geological Setting, Palaeoenvironment and Archaeology of the Red Sea*. *Springer Earth System Science Series, Springer Nature, Cham*, 131-157, doi: 10.1007/978-3-319-99408-6_7.

Lissenberg, C.J. & Dick, H.J.B. (2008). Melt-rock reaction in the lower oceanic crust and its implications for the genesis of mid-ocean ridge basalt. *Earth and Planetary Science Letters* **271**, 311-325, doi: 10.1016/j.epsl.2008.04.023.

Lissenberg, C.J., MacLeod, C.J., Howard, K.A., Godard, M. (2013). Pervasive reactive melt migration through fast-spreading lower oceanic crust (Hess Deep, equatorial Pacific Ocean). *Earth and Planetary Science Letters* **361**, 436–447, doi: 10.1016/j.epsl.2012.11.012.

Lissenberg, C.J., MacLeod, C.J. & Bennett, E.N. (2019). Consequences of a crystal mush-dominated magma plumbing system: a mid-ocean ridge perspective. *Philosophical Transactions of the Royal Society A* **377**, 20180014, doi: 10.1098/rsta.2018.0014.

Lowell, J.D. & Genik, G.J. (1972). Sea-floor spreading and structural evolution of southern Red Sea. *The American Association of Petroleum Geologists Bulletin* **56**, 247-259.

Manighetti, I., Tapponnier, P., Courtillot, V., Gruszow, S. & Gillot, P.Y. (1997). Propagation of rifting along the Arabia-Somalia plate boundary: the Gulfs of Aden and Tadjoura. *Journal of Geophysical Research* **102**, 2681-2710.

Mattash, M.A., Pinarelli, L., Vaselli, O., Minissale, A., Jaimes-Viera, M.C., Al-Kadasi, M., Shawki, M.N. & Tassi, F. (2014). Geochemical evolution of southern Red Sea and Yemen flood volcanism: evidence for mantle heterogeneity. *Arabian Journal of Geosciences* **7**, 4831-4850.

McGuire, A.V. & Coleman R.G. (1986). The Jabal Tirf layered gabbro and associated rocks of the Tihama Asir complex, SW Saudi Arabia. *Journal of Geology* **94**, 651-665.

McLennan, S.M. (2001). Relationships between the trace element composition of sedimentary rocks and upper continental crust. *Geochemistry, Geophysics, Geosystems* **2**, 2000GC000109, doi: 10.1029/2000GC000109.

Meurer, W.P. & Boudreau, A.E. (1998). Compaction of Igneous Cumulates Part II: Compaction and the Development of Igneous Foliations. *Journal of Geology* **106**, 293-304, doi: 10.1086/516023.

Milanovsky, E.E. (1972). Continental rift zones: their arrangement and development. *Tectonophysics* **15**, 65–70, doi:10.1016/0040-1951(72)90052-2.

Miller, D.J., Abratis, M., Christie, D., Drouin, M., Godard, M., Ildefonse, B., Maeda, J., Weinsteiger, A., Yamasaki, T., Suzuki, Y., Niino, A., Sato, Y. & Takeda, F. (2009). Data report: microprobe analyses of primary mineral phases from site U1309, Atlantis Massif, IODP Expedition 304/305. In: *Blackman, D.K., Ildefonse, B., John, B.E., Ohara, Y., Miller, D.J., MacLeod, C.J. and the Expedition 304/305 Scientists (Eds.) Proceedings of the International Ocean Drilling Program*, **Vol. 304/305**. College Station, TX: Integrated Ocean Drilling Program, p. 4.

Mohriak, W. U., & Leroy, S. (2013). Architecture of rifted continental margins and break-up evolution: Insights from the South Atlantic, North Atlantic and Red Sea–Gulf of Aden conjugate margins. *Geological Society of London, Special Publications* **369** (1), 497–535.

Moucha, R. & Forte, A.M. (2011). Changes in African topography driven by mantle convection. *Nature Geosciences* **4**, 707-712, doi: 10.1038/ngeo1235.

Nachit, H., Ibhi, A., Abia, E.H. & Ohoud, M.B. (2005). Discrimination between primary magmatic biotites, reequilibrated biotites and neoformed biotites. *C.R. Geoscience* **337**, 1415-1420.

Namur, O., Abily, B., Boudreau, A.E., Blanchette, F., Bush, J.W.M., Ceuleneer, G., Charlier, B., Donaldson, C.H., Duchesne, J.-C., Higgins, M.D., Morata, D., Nielsen, T.F.D., O'Driscoll, B.O., Pang, K.N., Peacock, T., Spandler, C.J., Toramaru, A. & Veksler, I.V. (2015). Igneous layering in basaltic magma chambers. In: *Charlier et al. (Eds.) Layered Intrusions*, Springer Geology, 75-152, doi: 10.1007/978-94-017-9652-1_2.

Natland, J.H. & Dick, H.J.B. (2002). Stratigraphy and composition of gabbros drilled in Ocean Drilling Program Hole 735B, Southwest Indian Ridge: A synthesis of geochemical data. In: *Natland, J.H., Dick, H.J.B., Miller, D.J., and Von Herzen, R.P. (Eds.), Proceedings of the Ocean Drilling Program, Scientific Results*, **176**, 1–69.

Nguyen, D.K., Morishita, T., Soda, Y., Tamura, A., Ghosh, B., Harigane, Y., France, L., Liu, C., Natland, J.H., Sanfilippo, A., MacLeod, C.J., Blum, P. & Dick, H.J.B. (2018). Occurrence of felsic rocks in oceanic gabbros from IODP Hole U1473A: Implications for evolved melt migration in the lower oceanic crust. *Minerals* **8**, 583, doi: 10.3390/min8120583.

Pallister, J.S., Stacey J.S., Fischer, L.B. & Premo, W.R. (1987). Arabian shield ophiolites and late Proterozoic microplate accretion. *Geology* **15**, 320–323.

Petrunin, A. G., Kaban, M. K., El Khrepy, S. & Al-Arifi, N. (2020). Mantle convection patterns reveal the mechanism of the Red Sea rifting. *Tectonics* **39**, e2019TC005829, doi: 10.1029/2019TC005829.

Phillips, J.D. (1970). Magnetic anomalies in the Red Sea. *Philosophical Transactions of the Royal Society of London. Series A, Mathematical and Physical Sciences* **267**, 205–217.

Rampone, E., Borghini, G. & Basch, V. (2020). Melt migration and melt-rock reaction in the Alpine-Apennine peridotites: Insights on mantle dynamics in extending lithosphere. *Geoscience Frontiers* **11**, 151-166.

Roger, J., Platel, J.P., Cavelier, C. & Bourdillon-de-Grisac, C. (1989). Données nouvelles sur la stratigraphie et l'histoire géologique du Dhofar (Sultanat d'Oman). *Bulletin de la Société Géologique de France* **8**, 265-277.

Röser, H.A. (1975). A detailed magnetic survey of the southern Red Sea. *Geologische Jahrbuch* **13**, 131-153.

Sahota, G. (1990). Geophysical investigations of the Gulf of Aden continental margins: geodynamic implications for the development of the Afro-Arabian Rift system. *PhD thesis, University College, Swansea, UK.*

Sanfilippo, A., Tribuzio, R. & Tiepolo, M. (2014). Mantle–crust interactions in the oceanic lithosphere: Constraints from minor and trace elements in olivine. *Geochimica et Cosmochimica Acta* **141**, 423-439.

Sanfilippo, A., Dick, H.J.B., Ohara, Y. & Tiepolo, M. (2016). New insights on the origin of troctolites from the breakaway area of the Godzilla Megamullion (Parece Vela back-arc

basin): The role of melt-mantle interaction on the composition of the lower crust. *Island Arc*, **25**, 220–234, doi: 10.1111/iar.12137.

Sanfilippo, A., Cai, Y., Gouveia Jácome, A.P. & Ligi, M. (2019). Geochemistry of the Lunayyir and Khaybar Volcanic Fields (Saudi Arabia): Insights into the Origin of Cenozoic Arabian Volcanism. In: *Rasul, N.M.A. and Stewart, I.C.F. (Eds.) Geological Setting, Palaeoenvironment and Archaeology of the Red Sea*, *Springer Earth System Science Series, Springer Nature, Cham, 389-415,* doi: 10.1007/978-3-319-99408-6_18.

Sanfilippo, A., MacLeod, C.J., Tribuzio, R., Lissenberg, C.J. & Zanetti, A. (2020). Early-stage melt-rock reaction in a cooling crystal mush beneath a slow-spreading mid-ocean ridge (IODP Hole U1473A, Atlantis Bank, Southwest Indian Ridge). *Frontiers in Earth Science*, **8**, 579138, doi: 10.3389/feart.2020.579138.

Schmidt, D.L., Hadley, D.G. & Brown, G.F. (1982). Middle Tertiary continental rift and evolution of the Red Sea in southwestern Saudi Arabia. *Saudi Arabian Deputy Ministry of Mineral Resources*, USGS-OF-03-6, pp. 56.

Searle, R.C. & Ross, D.A. (1975). A geophysical study of the Red Sea axial trough between 20.5° and 22°N. *Geophysical Journal of the Royal Astronomical Society* **43**:555–572.

Sebai, A., Zumbo, V., Féraud, G., Bertrand, H., Hussain, A.G., Giannérini, G. & Campredon, R. (1991). $^{40}Ar/^{39}Ar$ dating of alkaline and tholeiitic magmatism of Saudi Arabia related to the early Red Sea Rifting. *Earth and Planetary Science Letters* **104**, 473-487. doi:10.1016/0012-821X(91)90223-5.

Sparks, R.S.J., Annen, C., Blundy, J.D., Cashman, K.V., Rust, A.C. & Jackson, M.D. (2019). Formation and dynamics of magma reservoirs. *Philosophical Transactions of the Royal Society A* **377**, 20180019, doi: 10.1098/rsta.2018.0019.

Stern, R.J. & Johnson, P. (2010). Continental lithosphere of the Arabian Plate: a geologic, petrologic, and geophysical synthesis. *Earth Science Reviews* **101**, 29–67. doi:10.1016/j.earscirev.2010.01.002.

Stern, R.J. & Johnson, P. (2019). Constraining the Opening of the Red Sea: Evidence from the Neoproterozoic Margins and Cenozoic Magmatism for a Volcanic Rifted Margin. In: *Rasul, N.M.A. and Stewart, I.C.F. (Eds.) Geological Setting, Palaeoenvironment and Archaeology of the Red Sea, Springer Earth System Science Series, Springer Nature, Cham*, 53-79, doi: 10.1007/978-3-319-99408-6_4.

Sultan, M., Becker, R., Arvidson, R. E., Shore, P., Stern, R. J., El Alfy, Z. & Guinness, E. A. (1992). Nature of the Red Sea crust: a controversy revisited. *Geology* **20**, 593.

Sun, C. & Liang, Y. (2017). A REE-in-plagioclase–clinopyroxene thermometer for crustal rocks. *Contributions to Mineralogy and Petrology* **172**, 24, doi: 10.1007/s00410-016-1326-9.

Sun, S.S. & McDonough, W.F. (1989). Chemical and isotopic systematics of oceanic basalts: implications for mantle composition and processes. *Geological Society of London, Special Publications* **42**, 313-345, doi: 10.1144/GSL.SP.1989.042.01.19.

Thybo, H. & Nielsen, C.A. (2009). Magma-compensated crustal thinning in continental rift zones. *Nature*, **457**, 873-876, doi: 10.1038/nature07688.

van der Zwan, F. M., Devey, C. W., Augustin, N., Almeev, R. R., Bantan, R. A. & Basaham, A. (2015). Hydrothermal activity at the ultraslow- to slow-spreading Red Sea Rift traced by chlorine in basalt. *Chemical Geology* **405**, 63-81, doi: 10.1016/j.chemgeo.2015.04.001.

Voggenreiter, W., Hötzl, H. & Jado, A.R. (1988). Red Sea related history of extension and magmatism in the Jizan area (southwest Saudi Arabia): indication for simple-shear rifting. *Geol. Rundsch* **71**, 257-274.

Voss, M. & Jokat, W. (2007). Continent-ocean transition and voluminous magmatic underplating derived from P-wave velocity modeling of the East Greenland continental margin. *Geophysical Research Letters* **170**, 580-604.

Watchorn, F., Nichols, G.J. & Bosence, D.W.J. (1998). Rift-related sedimentation and stratigraphy, southern Yemen (Gulf of Aden). In: *Purser, B.H. and Bosence, D.W.J. (Eds.) Sedimentation and tectonics of rift basins: Red Sea-Gulf of Aden*. Chapman and Hall, London, 165–189.

Whitney, D.L. & Evans, B.W. (2010). Abbreviations for Names of Rock-Forming Minerals. *American Mineralogist* **95**, 185-187, doi: 10.2138/am.2010.3371.

Woodruff, F. & Savin, S.M. (1989). Miocene deepwater oceanography. *Paleoceanography* **4**, 87-140.

Workman, R.K. & Hart, S.R. (2005). Major and trace element composition of the depleted MORB mantle (DMM). *Earth and Planetary Science Letters* **231**, 53-72, doi: 10.1016/j.epsl.2004.12.005

Wright, T., Sigmundsson, F., Ayele, A., Belachew, M., Brandsdottir, B., Calais, E., Ebinger, C., Einarsson, P., Hamling, I., Keir, D., Lewi, E., Pagli, C. & Pedersen, R. (2012). Geophysical constraints on the dynamics of spreading centres from rifting episodes on land. *Nature Geoscience* **5**, 242–250, doi: 10.1038/ngeo1428.

Zahran, H.M., Stewart, I.C.F., Johnson, P.R. & Basahel, M.H. (2003). Aeromagnetic-anomaly maps of central and western Saudi Arabia. Scale 1:2 million. *Saudi Geological Survey Open-File Report SGS-OF-2002-8*, 6 p., 4 plates.

Table 1: Studied samples, sample location, lithotype and modal compositions

| | | | | | Modal composition (vol%) | | | | | | | |
|---|---|---|---|---|---|---|---|---|---|---|---|---|
| Sample | Location | Latitude | Longitude | Lithotype | Plg | Cpx | Ol | Ox | Amph | Bt | Opx | Matrix |
| TA01-Tlg1 | Masliyah | 17°26'10" N | 42°35'57" E | Por. gabbro | 45 | 0 | 0 | 0 | 0 | 0 | 0 | 55 |
| TA02-Tlg3 | Masliyah | 17°26'10" N | 42°35'57" E | Por. gabbro | 40 | 0 | 0 | 0 | 0 | 0 | 0 | 60 |
| TA02-Tlg5 | Masliyah | 17°26'10" N | 42°35'57" E | Cpx-gabbro | 63 | 25 | 0 | 10 | 2 | 0 | 0 | 0 |
| TA02/Dy-1 | Masliyah | 17°26'10" N | 42°35'57" E | Basalt | 12 | 4 | 0 | 1 | 0 | 0 | 0 | 83 |
| TA03-Tgg1 | Masliyah | 17°26'20" N | 42°36'52" E | Cpx-gabbro | 69 | 20 | 0 | 5 | 1 | 0 | 5 | 0 |
| TA03-Tgg3 | Masliyah | 17°26'20" N | 42°36'52" E | Por. gabbro | 40 | 0 | 0 | 0 | 0 | 0 | 0 | 60 |
| TA03-Tgg4 | Masliyah | 17°26'20" N | 42°36'52" E | Cpx-gabbro | 72 | 20 | 0 | 7 | 1 | 0 | 0 | 0 |
| TA04-Tgg1 | Masliyah | 17°26'20" N | 42°37'24" E | Oxide gabbro | 40 | 35 | 4 | 16 | 1 | 4 | 0 | 0 |
| TA05-Tgg1 | Masliyah | 17°26'23" N | 42°37'40" E | Ol-gabbro | 55 | 24 | 20 | 1 | 0 | 0 | 0 | 0 |
| TA05-Tgg3 | Masliyah | 17°26'23" N | 42°37'40" E | Ol-gabbro | 50 | 25 | 24 | 1 | 0 | 0 | 0 | 0 |
| TA06-Tlg1 | Masliyah | 17°26'29" N | 42°35'49" E | Por. gabbro | 40 | 0 | 0 | 0 | 0 | 0 | 0 | 60 |
| TA-06/Dy-1 | Masliyah | 17°26'29" N | 42°35'49" E | Basalt | 9 | 2 | 0 | 1 | 0 | 0 | 0 | 88 |
| TA07-Tlg2 | Jabal al Tirf | 16°59'23" N | 42°57'20" E | Cpx-gabbro | 55 | 35 | 2 | 6 | 2 | 0 | 0 | 0 |
| TA07-Tlg3 | Jabal al Tirf | 16°59'23" N | 42°57'20" E | Ol-gabbro | 50 | 35 | 10 | 3 | 1 | 0 | 1 | 0 |
| TA08-Tlg1 | Jabal al Tirf | 16°59'19" N | 42°57'23" E | Ol-gabbro | 55 | 30 | 8 | 5 | 2 | 0 | 0 | 0 |
| TA08-Tlg3 | Jabal al Tirf | 16°59'19" N | 42°57'23" E | Cpx-gabbro | 52 | 40 | 0 | 7 | 1 | 0 | 0 | 0 |
| TA09-Tlg1 | Jabal al Tirf | 16°59'21" N | 42°57'22" E | Ol-gabbro | 50 | 30 | 10 | 7 | 3 | 0 | 0 | 0 |
| TA-15/Tgb-1 | Jabal Sawdah | 17°30'42" N | 42°28'33" E | Basalt | 9 | 3 | 0 | 1 | 0 | 0 | 0 | 87 |
| TA-16/Tgb-1 | Jabal Sawdah | 17°30'42" N | 42°28'33" E | Basalt | 11 | 4 | 0 | 1 | 0 | 0 | 0 | 84 |
| TA-16/Tgb-3 | Jabal Sawdah | 17°30'42" N | 42°28'33" E | Basalt | 14 | 5 | 0 | 1 | 0 | 0 | 0 | 80 |
| TA-16/Tgb-5 | Jabal Sawdah | 17°30'42" N | 42°28'33" E | Basalt | 12 | 3 | 0 | 1 | 0 | 0 | 0 | 84 |
| TA-17/Tgb-2 | Jabal Sawdah | 17°31'21" N | 42°30'32" E | Basalt | 6 | 2 | 0 | 1 | 0 | 0 | 0 | 91 |
| TA-17/Tgb-3 | Jabal Sawdah | 17°31'21" N | 42°30'32" E | Basalt | 7 | 2 | 0 | 1 | 0 | 0 | 0 | 90 |
| TA-18/Tgb-2 | Jabal Sawdah | 17°31'21" N | 42°30'32" E | Basalt | 11 | 3 | 0 | 1 | 0 | 0 | 0 | 85 |
| TA-18/Tgb-4 | Jabal Sawdah | 17°31'21" N | 42°30'32" E | Basalt | 10 | 2 | 0 | 1 | 0 | 0 | 0 | 87 |
| TA-19/Tgb-1 | Jabal Sawdah | 17°31'27" N | 42°28'54" E | Basalt | 11 | 4 | 0 | 1 | 0 | 0 | 0 | 84 |
| TA-20/Tgb-1 | Jabal Sawdah | 17°31'27" N | 42°28'54" E | Basalt | 8 | 3 | 0 | 1 | 0 | 0 | 0 | 88 |
| TA-20/Tgb-3 | Jabal Sawdah | 17°31'27" N | 42°28'54" E | Basalt | 10 | 2 | 0 | 1 | 0 | 0 | 0 | 87 |
| TA-20/Tgb-5 | Jabal Sawdah | 17°31'27" N | 42°28'54" E | Basalt | 11 | 4 | 0 | 1 | 0 | 0 | 0 | 84 |

*Por. gabbro: Porphyric gabbro; Plg: plagioclase; Cpx: clinopyroxene; Ol: olivine; Ox: Fe-Ti oxide; Amph: amphibole; Bt: biotite; Opx: orthopyroxene; Matrix: microcrystalline matrix.*

**Figure captions:**

**Figure 1:** a) Distribution of Cenozoic to Quaternary volcanism in the Red Sea rift system. The top right inset presents a simplified plate tectonic framework of the Red Sea/Gulf of Aden area, in which green lines are oceanic spreading centers. Redrawn after Ligi *et al.* (2012) and Stern & Johnson (2019). The red box locates the Tihama Asir igneous complex; b) Geological map of the Tihama Asir igneous complex. The studied samples were collected in the Jabal al Tirf and Masliyah plutons, and in the Jabal Sawdah dike swarm. Redrawn after Stern & Johnson (2019).

**Figure 2:** a) Detailed geological map of the Jabal al Tirf pluton in the Tihama Asir igneous complex. The location of the ENE-WSW cross section, showing field relationships of the different igneous units in the Jabal al Tirf pluton, is indicated by the A-B line. Redrawn after McGuire & Coleman (1986); b) Photograph of the contact between layered gabbros and crosscutting granophyre body; c) Contact between layered gabbro and porphyric gabbro, crosscut by basaltic dike; d) Basaltic intrusion within metamorphic continental host rock. The rim of the basaltic intrusion is characterized by chilled margins.

**Figure 3:** Representative photomicrographs of the studied lithologies; a) Olivine gabbro showing compositional layering between olivine-rich layer and clinopyroxene-oxide-rich layer; b) Olivine gabbro showing a weak foliation defined by the elongation of plagioclase crystals and intra-crystalline deformation features in plagioclase; Crossed-nicols polarized light photomicrograph; c) Cpx-gabbro showing a weak layering defined by the elongation of plagioclase crystals and oxide oikocryst including plagioclase and clinopyroxene chadacrysts associated with interstitial amphibole; d) Gabbronoritic aggregate (clinopyroxene, orthopyroxene, plagioclase) in cpx-gabbro; Crossed-nicols polarized light photomicrograph; e) Oxide gabbro characterized by the occurrence of millimetre-size interstitial biotite associated with interstitial oxides; f) Porphyric gabbro showing centimetre-size plagioclase phenocrysts embedded in clinopyroxene + plagioclase + oxide microcrystalline matrix. The porphyric shows an irregular straight contact with a basaltic dike. The bottom right inset shows the sample macroscopic porphyric texture. Abbreviations are after Whitney & Evans (2010).

**Figure 4:** Whole rock compositions of the Tihama Asir gabbros and basaltic intrusions; Mg# (mol%) vs. a) CaO (wt%); b) $K_2O$ (wt%); c) La (ppm); d) Y (ppm); e) $La_N/Y_N$, Primitive Mantle normalisation values after Sun & McDonough (1989); f) Sr (ppm); g) Nb (ppm); U

(ppm). Also shown for comparison are the bulk-rock compositions of the Red Sea gabbros (after Ligi *et al.*, 2018), Tihama Asir igneous complex (McGuire & Coleman, 1986) and the bulk-rock compositions of Mid-Atlantic ridge gabbros (after Godard *et al.*, 2009).

**Figure 5:** Bulk-rock trace element patterns of the Tihama Asir gabbros; a) CI-chondrite-normalised bulk-rock REE patterns; b) Primitive Mantle-normalised bulk-rock trace element patterns. Also shown for comparison are the bulk-rock compositions of the Red Sea gabbros (after Ligi *et al.*, 2018). Normalisation values are after Sun & McDonough (1989).

**Figure 6:** Average clinopyroxene, plagioclase and olivine major element compositions and covariations; a) $Mg\#_{cpx}$ vs. a) $TiO_{2\ cpx}$ (wt%); b) $Cr_2O_{3\ cpx}$ (wt%); c) $Mg\#_{cpx}$ vs. $An_{plagio}$; d) $Fo_{ol}$ (mol%) vs. $NiO_{ol}$ (wt%). Mineral compositions from the Red Sea gabbros (Ligi *et al.*, 2018) and the Mid-Atlantic ridge gabbros (Miller *et al.*, 2009) are shown as reference.

**Figure 7:** Trace element compositions of clinopyroxene in the Tihama Asir gabbroic samples.; $Yb_N$ vs. a) $La_N$; b) $La_N/Y_N$; c) $La_N/Sm_N$; d) $Th_N/Y_N$. Mineral compositions from the Red Sea gabbros (Ligi *et al.*, 2018) and the Mid-Atlantic ridge gabbros and troctolites (Drouin *et al.*, 2009; Ferrando *et al.*, 2020) are shown as reference. Normalisation values are after Sun & McDonough (1989).

**Figure 8:** CI-chondrite normalised REE patterns and Primitive Mantle-normalised trace element patterns of: a-b) clinopyroxene; c-d) plagioclase; and e-f) amphibole. Mineral compositions from the Red Sea gabbros (Ligi *et al.*, 2018) and the Mid-Atlantic ridge gabbros and troctolites (Drouin *et al.*, 2009; Ferrando *et al.*, 2020) are shown as reference. Normalisation values are after Sun & McDonough (1989).

**Figure 9:** a) Computed equilibrium temperature of clinopyroxene-plagioclase couples using the REE thermometer after Sun & Liang (2017), plotted against the clinopyroxene and plagioclase Y contents normalised to Primitive Mantle; b) clinopyroxene compositions from Figure 7, compared with the computed patterns of *in situ crystallization*, assuming different amounts of melt mass returned into the magma chamber after fractionation (Langmuir, 1989). Mineral/melt partition coefficients and normalisation values are after Basch *et al.* (2018) and Sun & McDonough (1989), respectively.

**Figure 10:** Melt compositions computed in equilibrium with clinopyroxene cores and rims from the Tihama Asir gabbroic samples. The compositional field of Mid-Atlantic ridge basalts and Red Sea basalts are shown for reference (Godard *et al.*, 2009; van der Zwan *et al.*,

2015). Mineral/melt partition coefficients and normalisation values are after Basch *et al.* (2018) and Sun & McDonough (1989), respectively.

**Figure 11:** CI-normalised REE and Primitive Mantle-normalised trace element patterns of melt compositions in equilibrium with clinopyroxenes from Figure 9, compared with the patterns of Assimilation-Fractional Crystallization (after De Paolo, 1981) of an N-MORB parental composition (Table S8) assimilating average Upper Continental Crust (a, b) and Lower Continental Crust (c, d) compositions (after McLennan, 2001). The top right insets display the starting melt composition and assimilated material. The assimilation ratio (assimilated mass/crystallized mass) is fixed at Ma/Mc = 0.5 for assimilation of UCC and at Ma/Mc = 0.8 for assimilation of LCC. Melt fraction F decreases from 1 to 0.1. Mineral/melt partition coefficients and normalisation values are after Bédard (1994) and Basch *et al.* (2018), and Sun & McDonough (1989), respectively.

**Figure 12:** Modeling of clinopyroxene trace element compositions computed in equilibrium with the reacted melt during Assimilation-Fractional Crystallization (after De Paolo, 1981) of an N-MORB parental composition (Table S8) assimilating average Upper Continental Crust and Lower Continental Crust compositions (after McLennan, 2001), at variable assimilation rates (0.1 < Ma/Mc < 0.95). a,e) $La_N$; b, f) $La_N/Y_N$; c,g) $La_N/Sm_N$; d, h) $Th_N/Y_N$. Clinopyroxene compositions from the Red Sea gabbros (Ligi *et al.*, 2018) and the Mid-Atlantic ridge gabbros and troctolites (Drouin *et al.*, 2009; Ferrando *et al.*, 2020) are shown as reference. Mineral/melt partition coefficients and normalisation values are after Bédard (1994) and Basch *et al.* (2018), and Sun & McDonough (1989), respectively.

**Figure 13:** CI-normalised bulk-rock REE compositions of the Jabal Sawdah and Masliyah extrusives, compared to the melts in equilibrium with the Tihama Asir gabbro clinopyroxene cores. Diabase dikes from the Jabal al Tirf are shown for comparison (Coleman & McGuire, 1986) and N-MORB, E-MORB, OIB compositions and normalisation values are after Sun & McDonough (1989).

**Figure 14:** Representative sketch of the geodynamic environment of formation of the Tihama Asir gabbroic bodies and dike swarm. The concomitant crystallization of the gabbroic crystal mush and assimilation of the host continental crust produces hybridized melts that were ultimately extracted and formed the dike swarm.

**Fig. 1.**

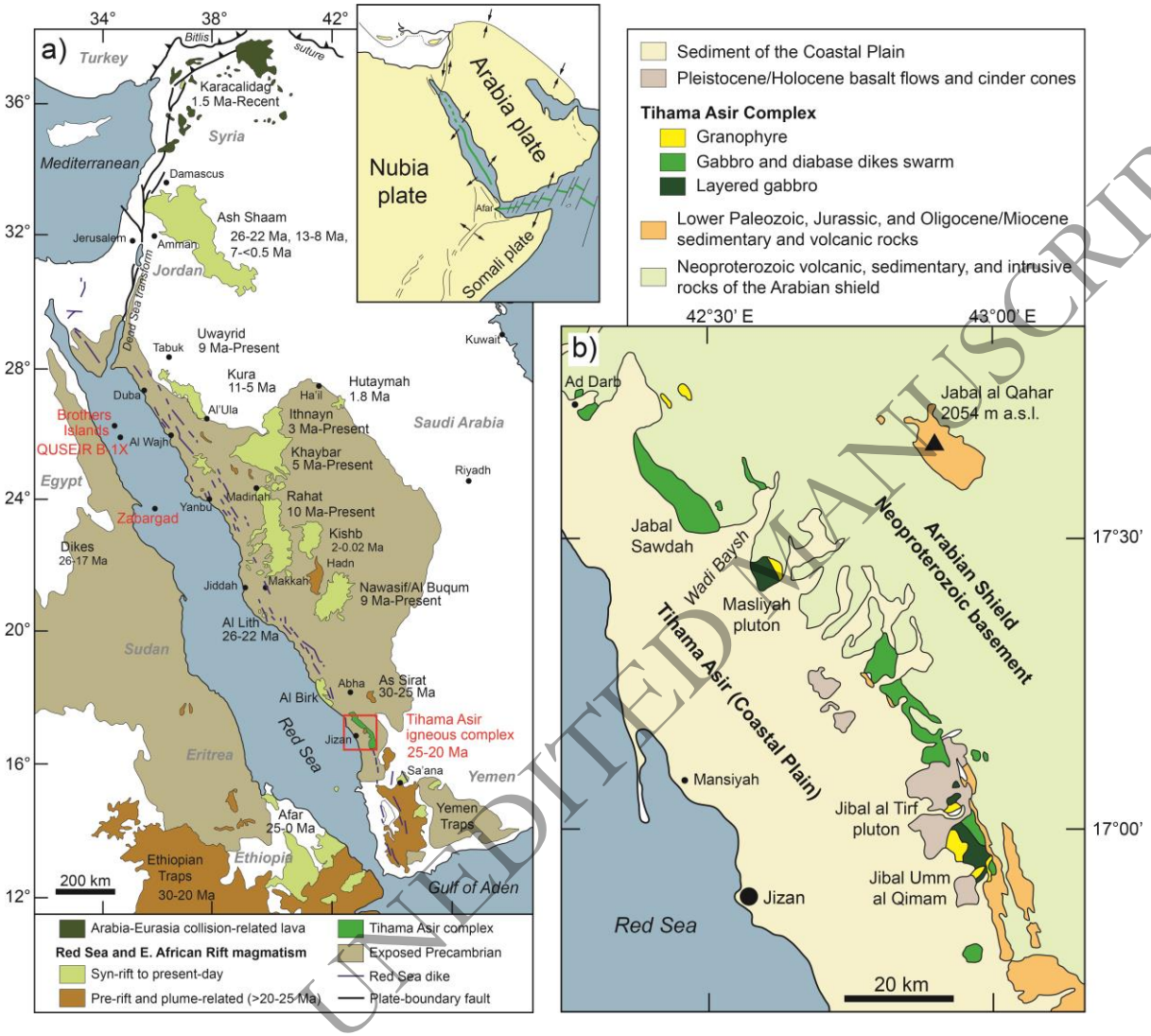

**Fig. 2.**

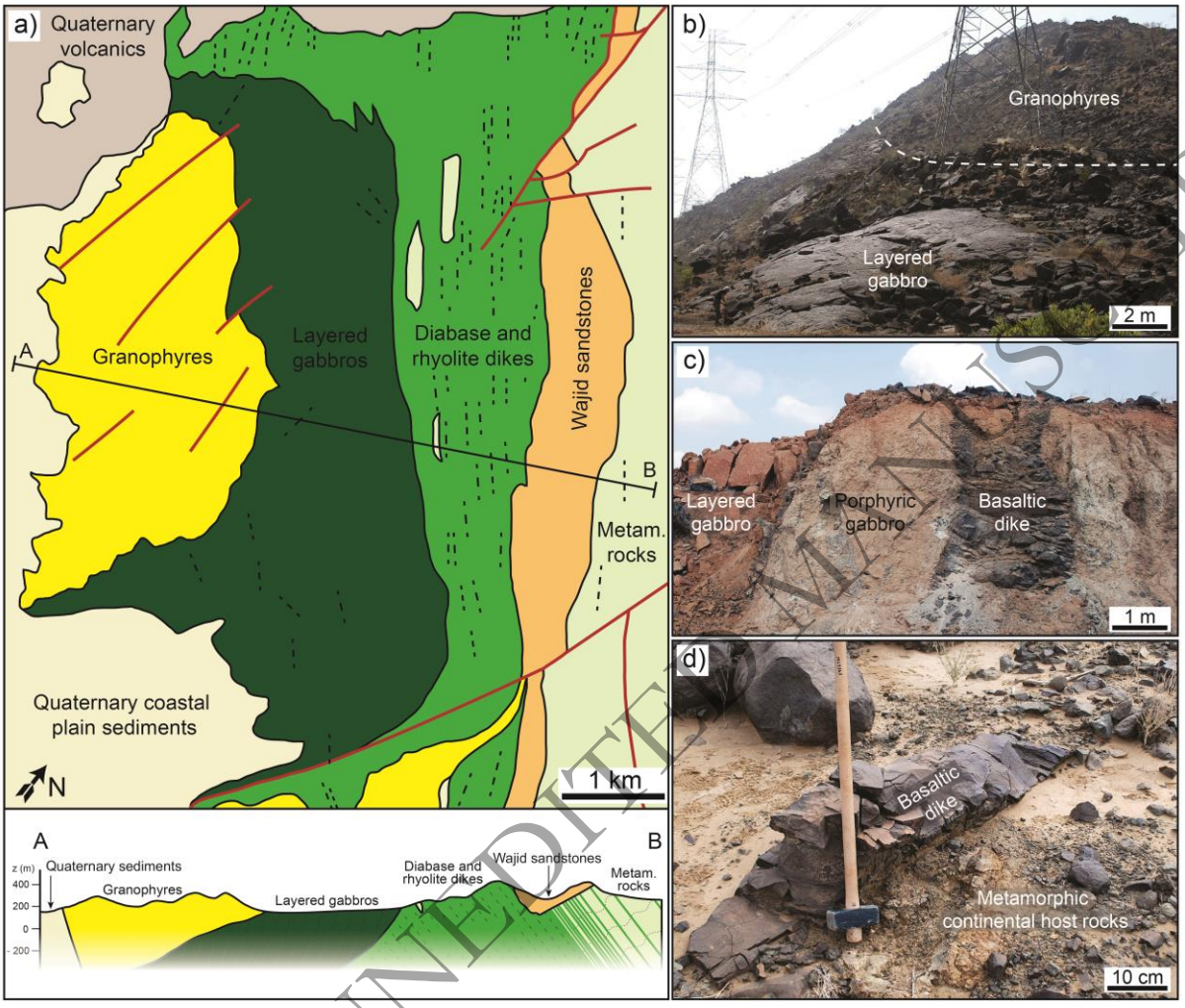

**Fig. 3.**

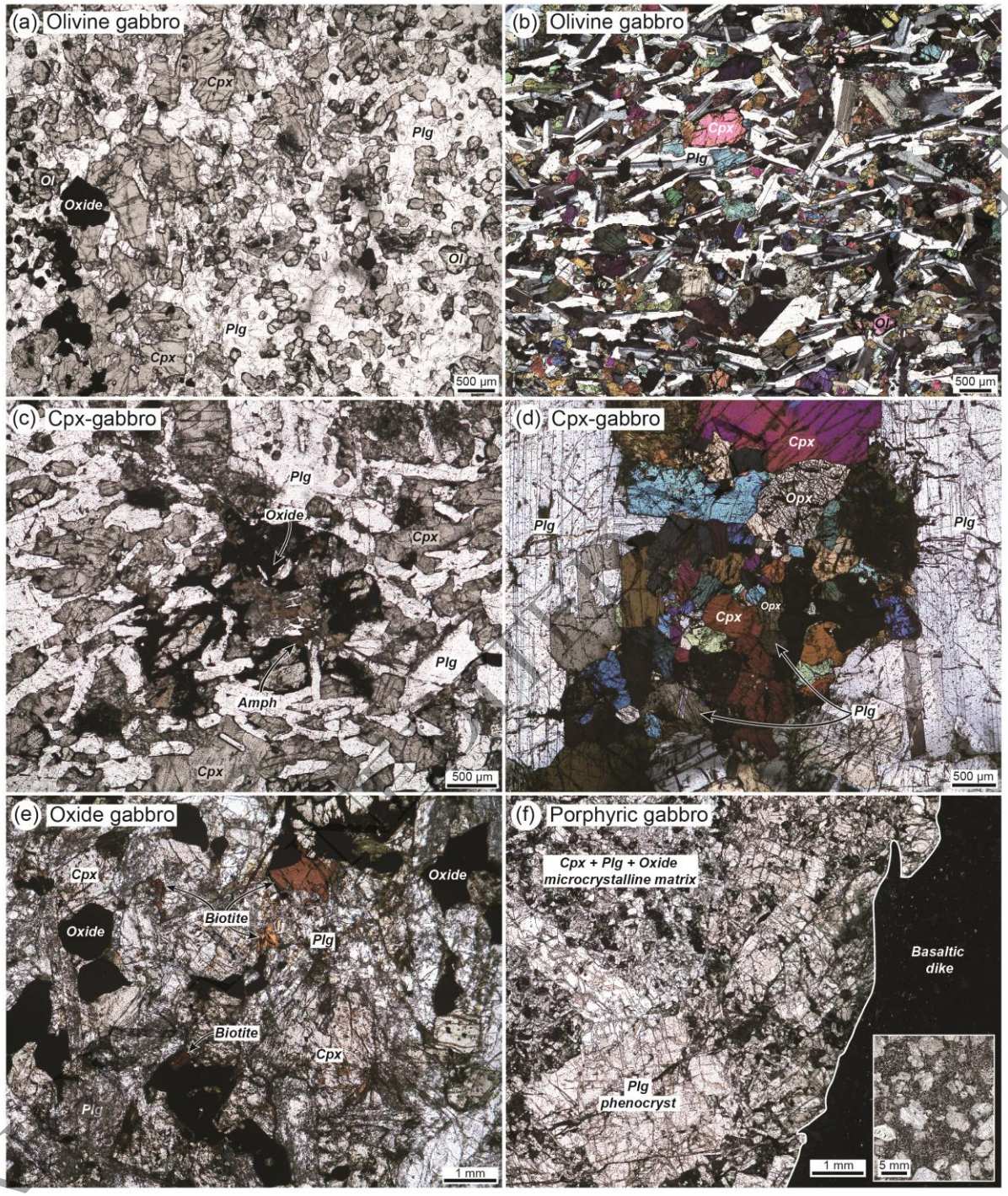

**Fig. 4.**

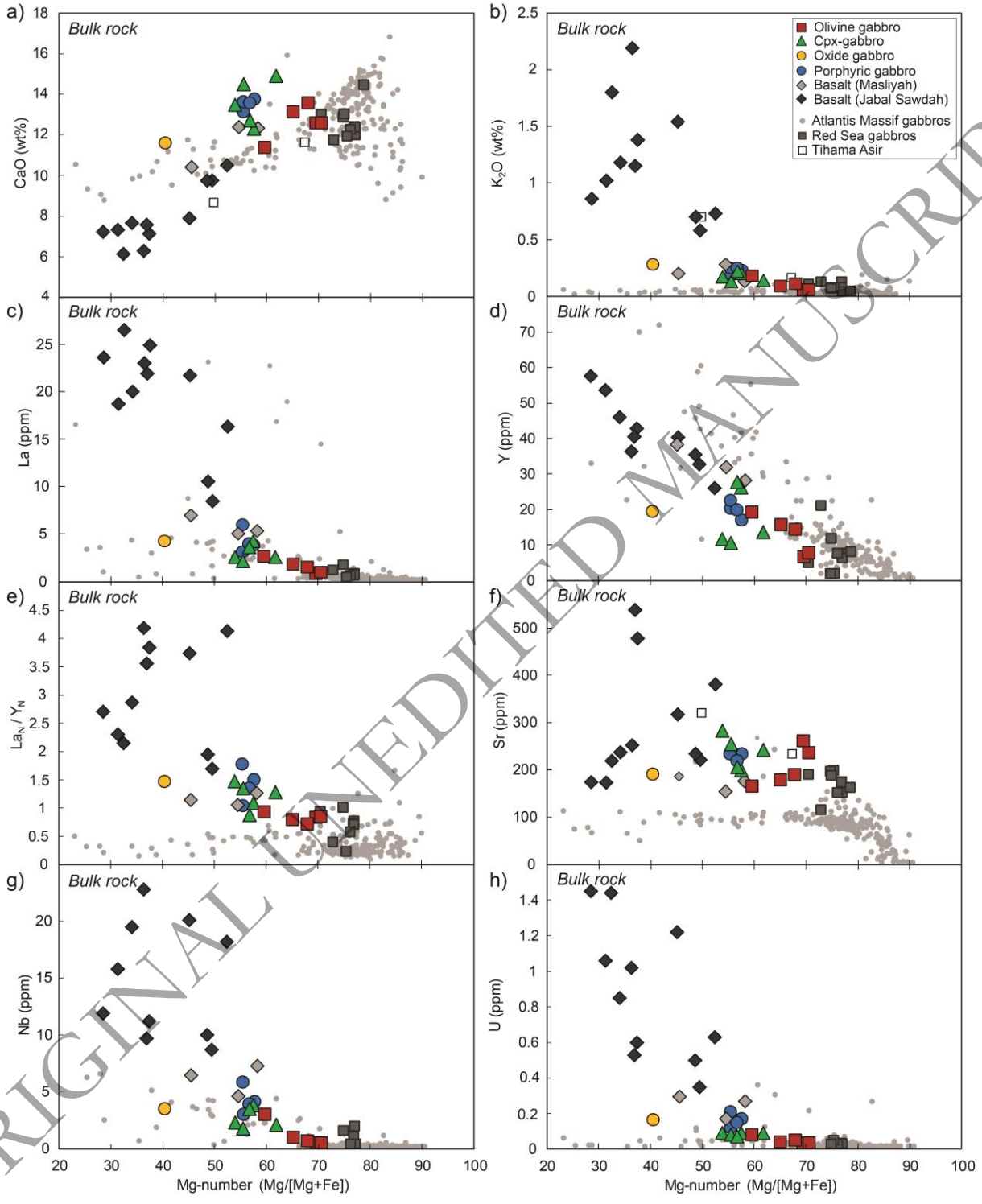

**Fig. 5.**

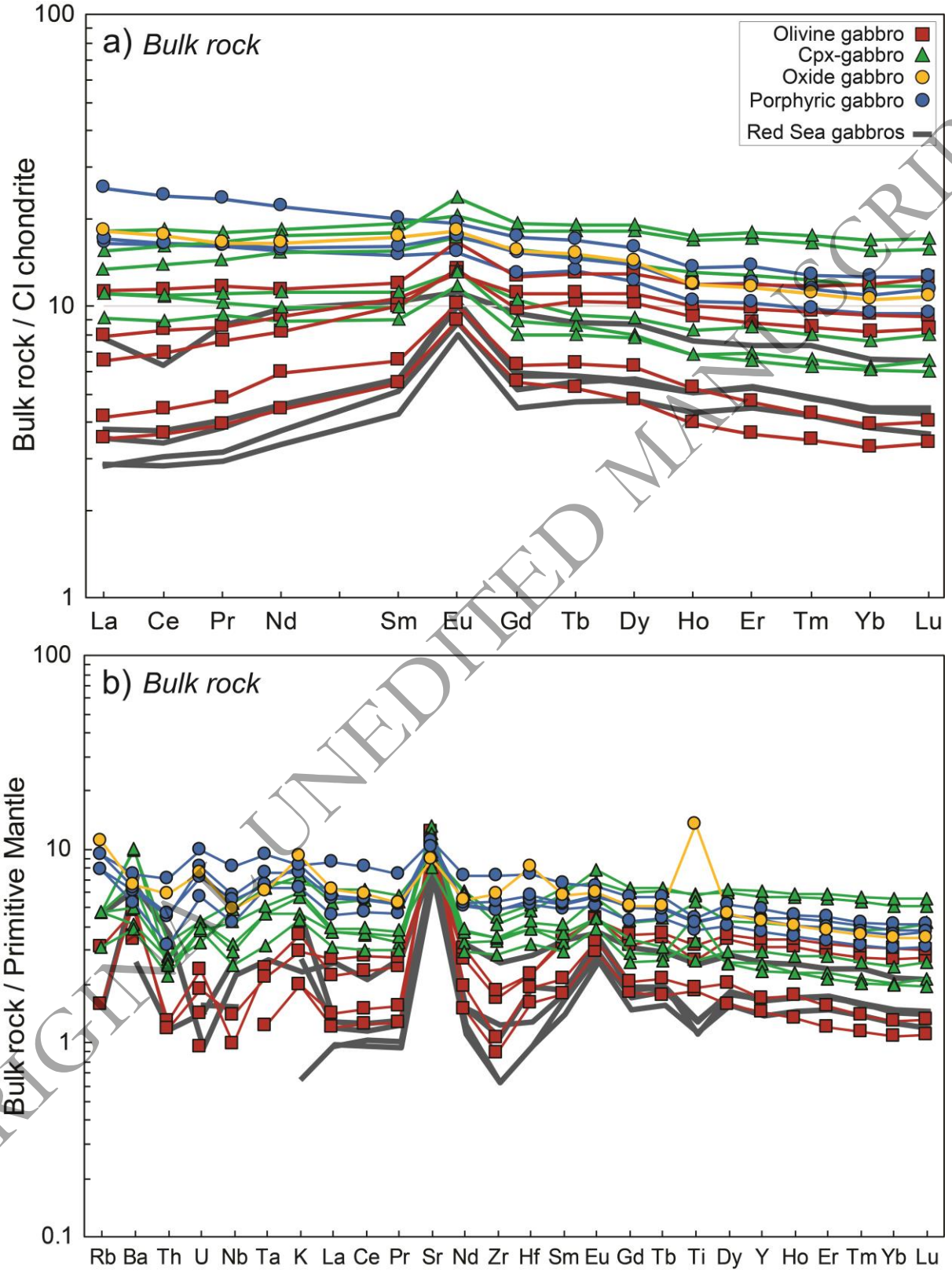

**Fig. 6.**

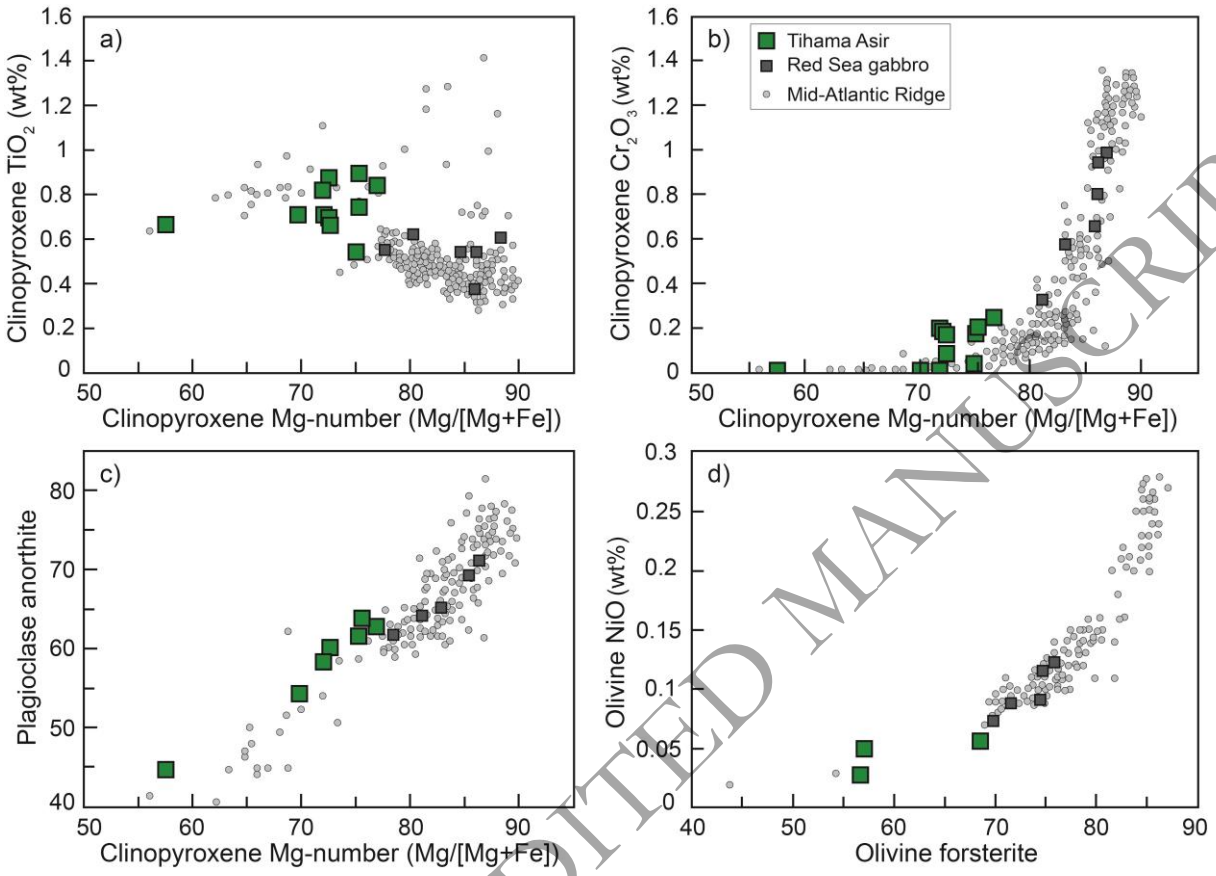

**Fig. 7.**

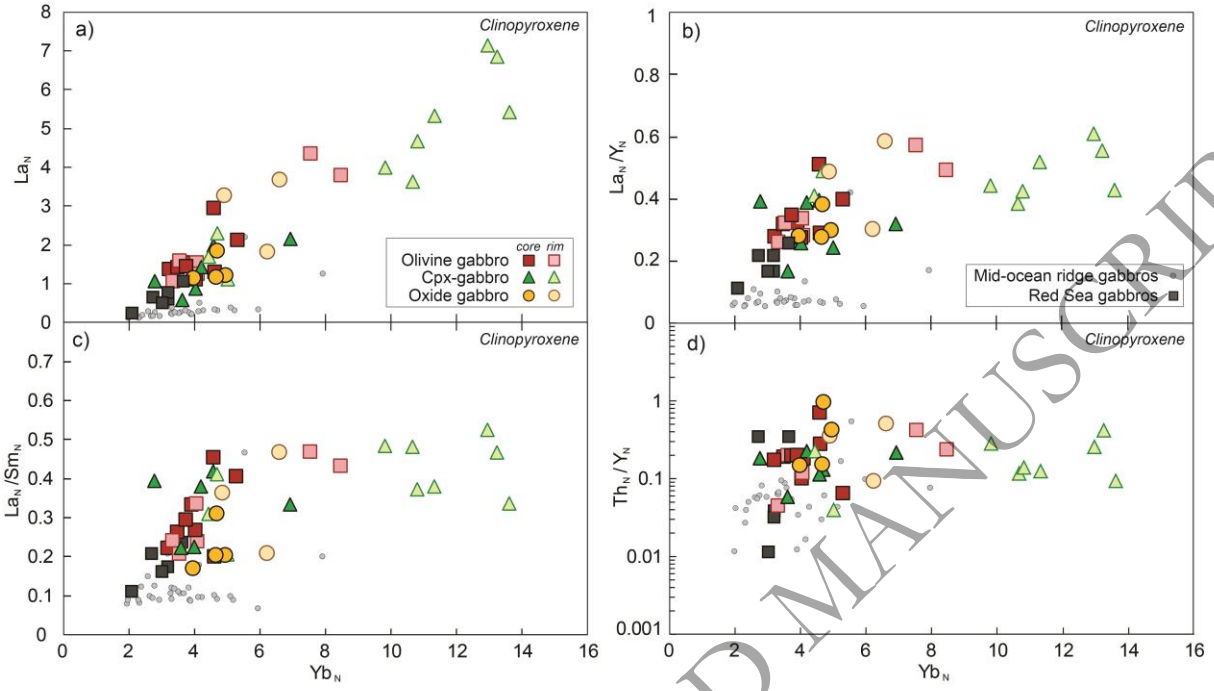

**Fig 8.**

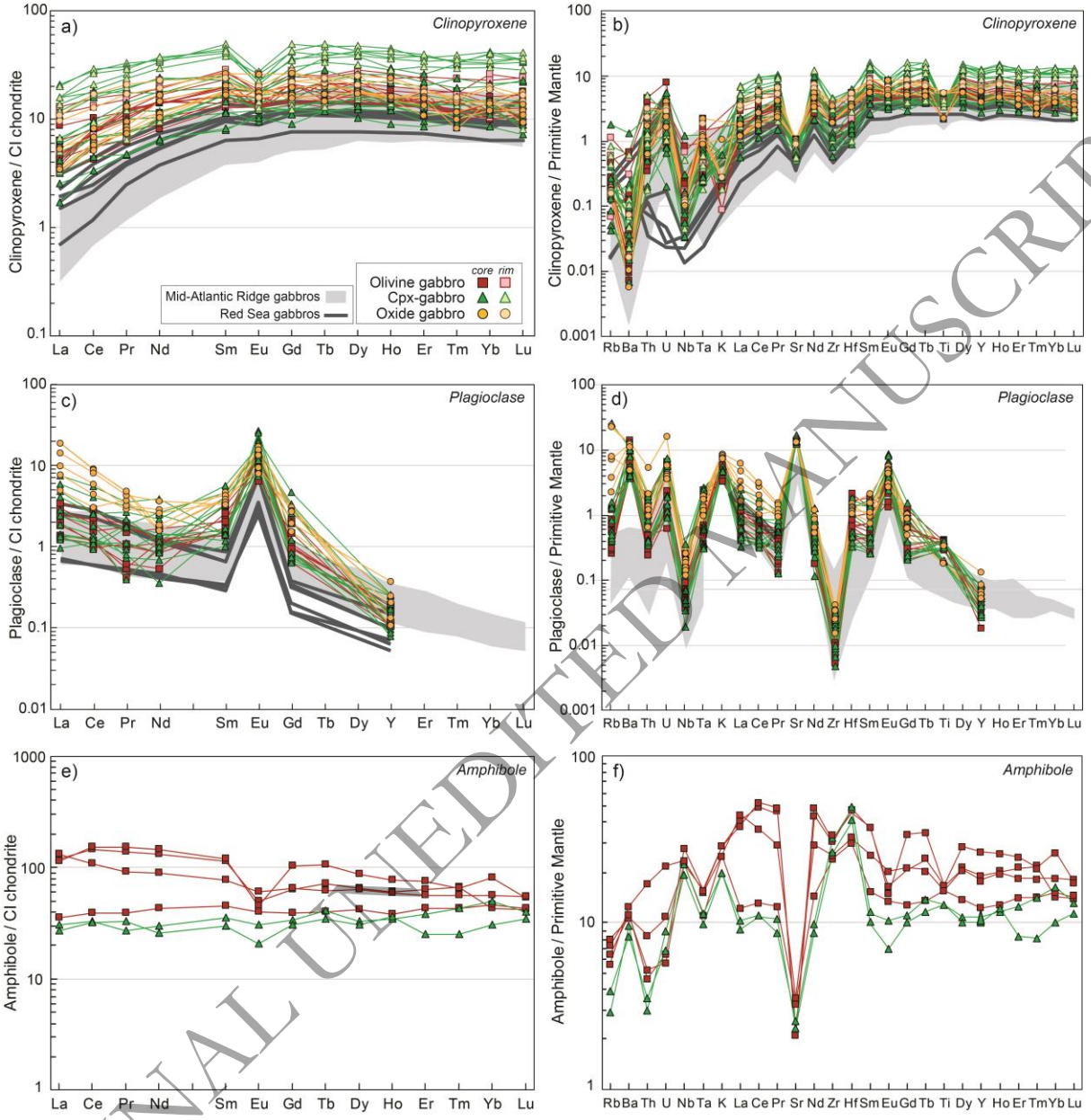

**Fig. 9.**

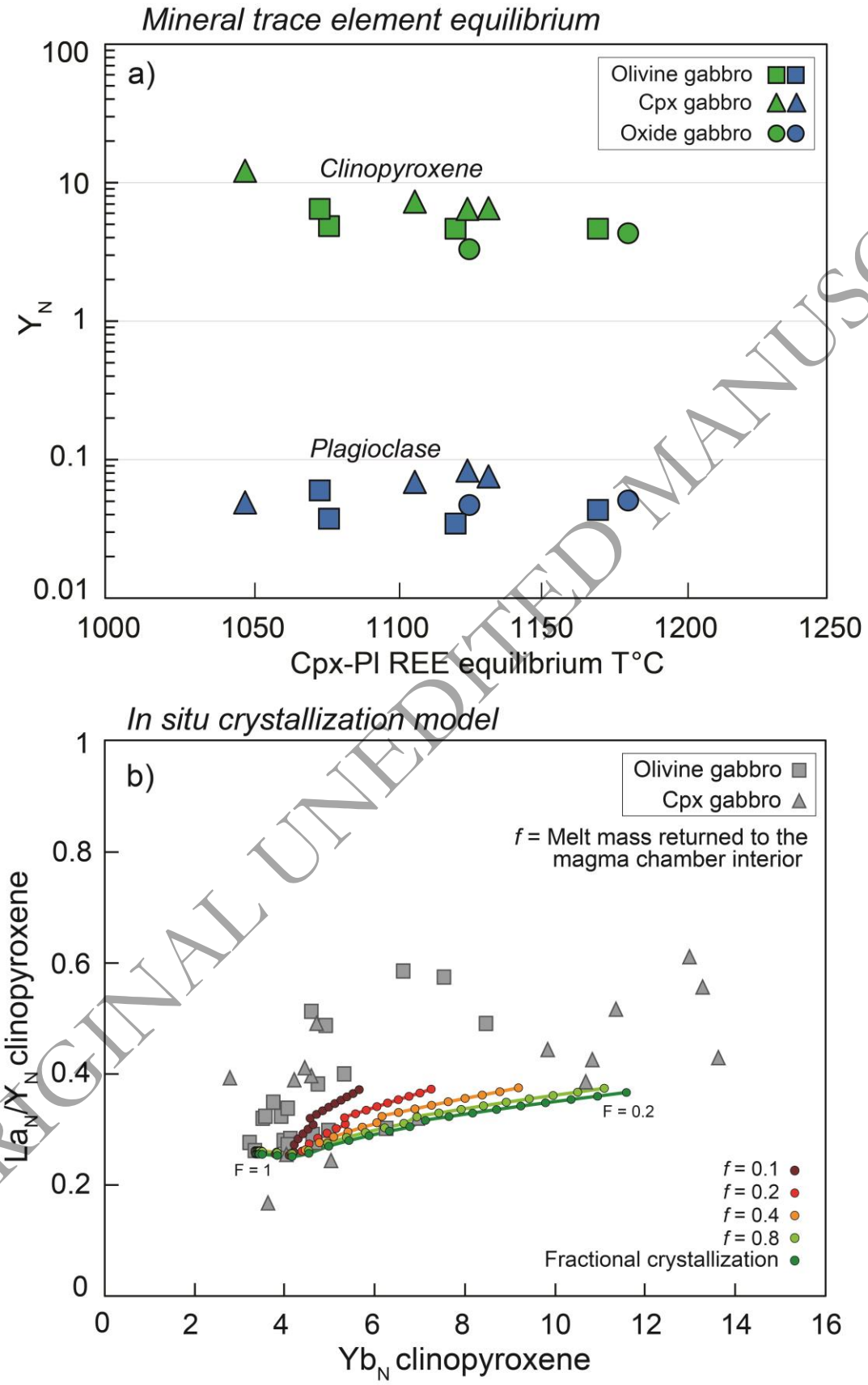

**Fig. 10.**

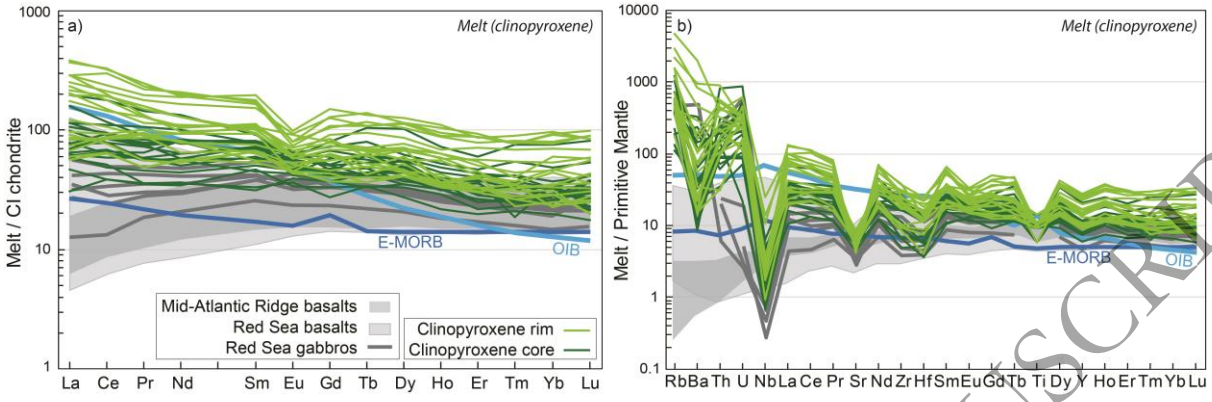


**Fig. 11.**

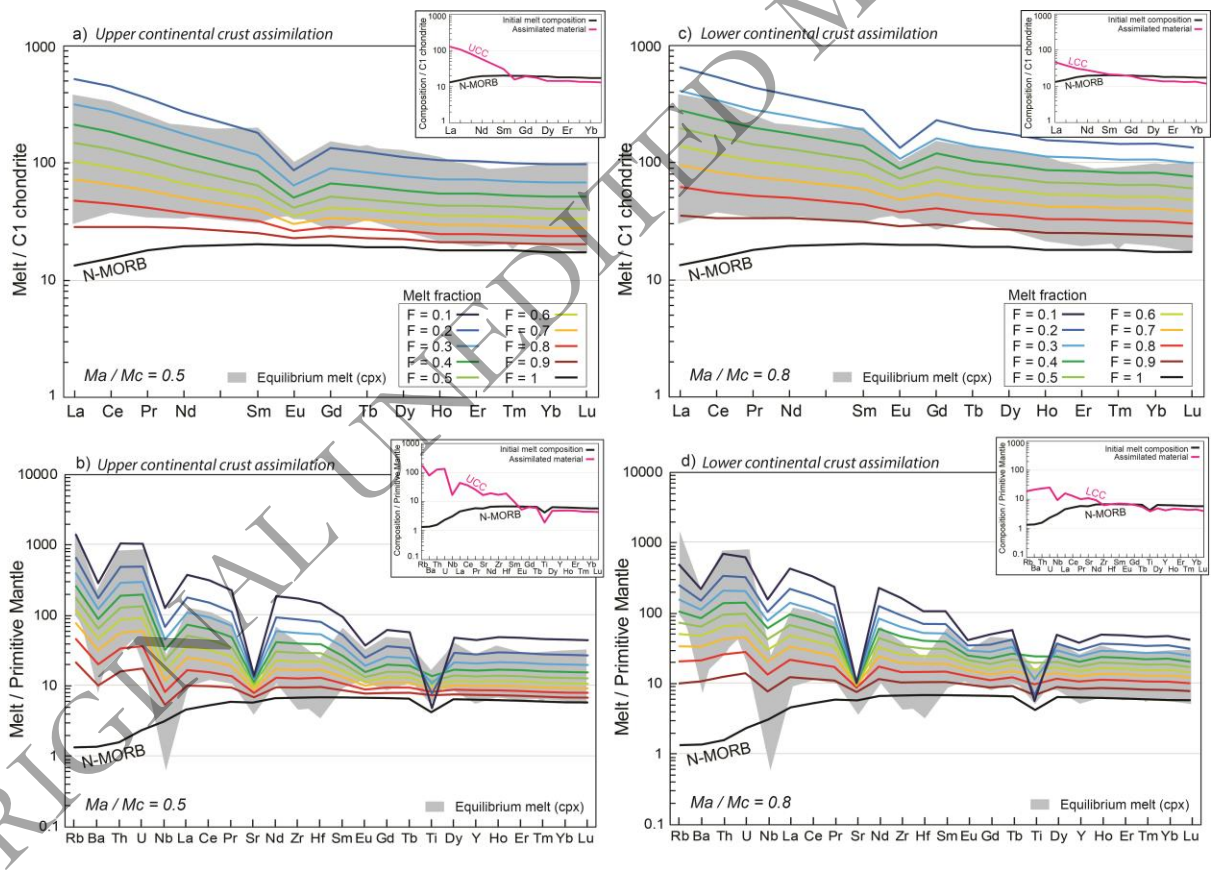

**Fig. 12.**

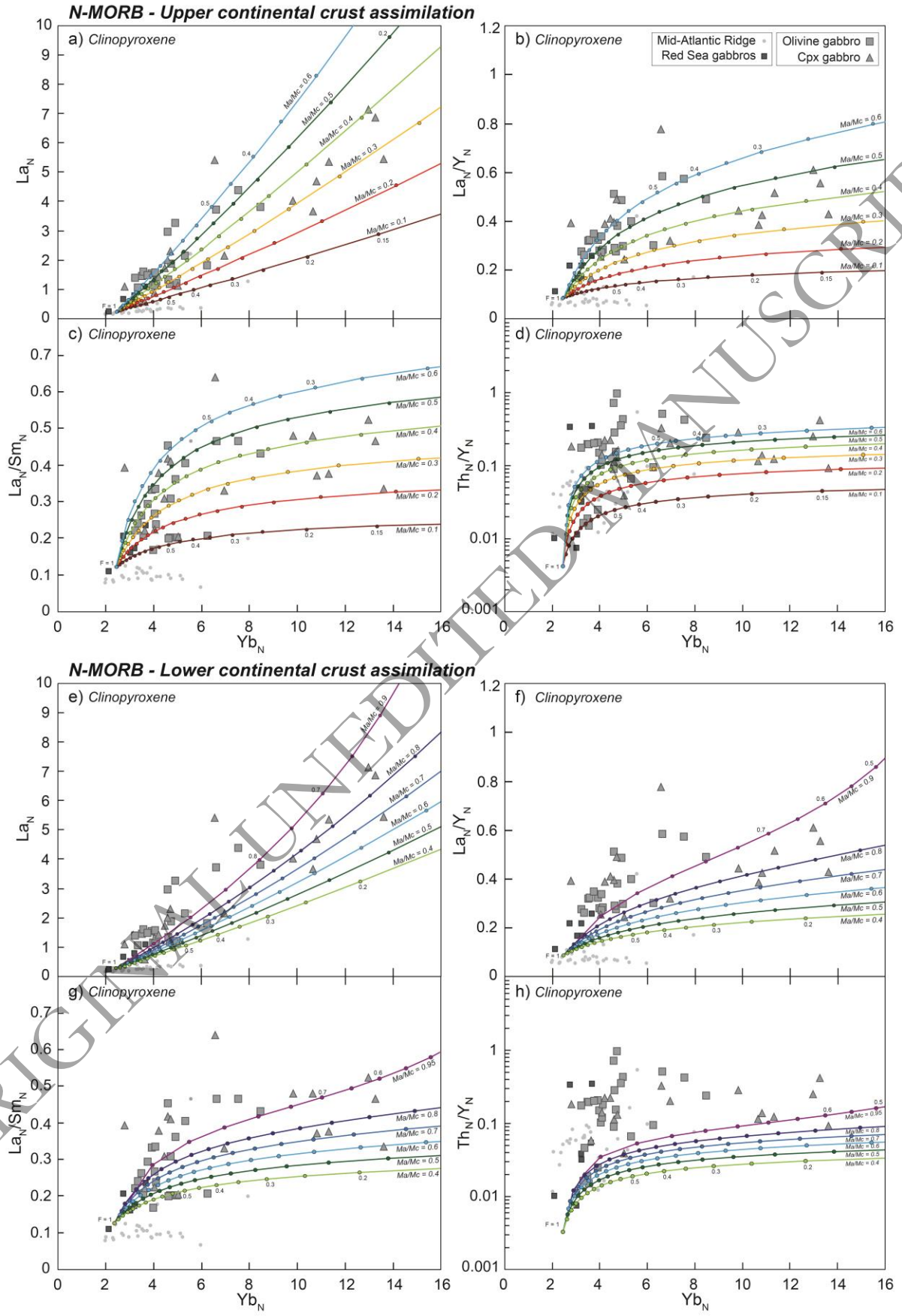

**Fig. 13.**

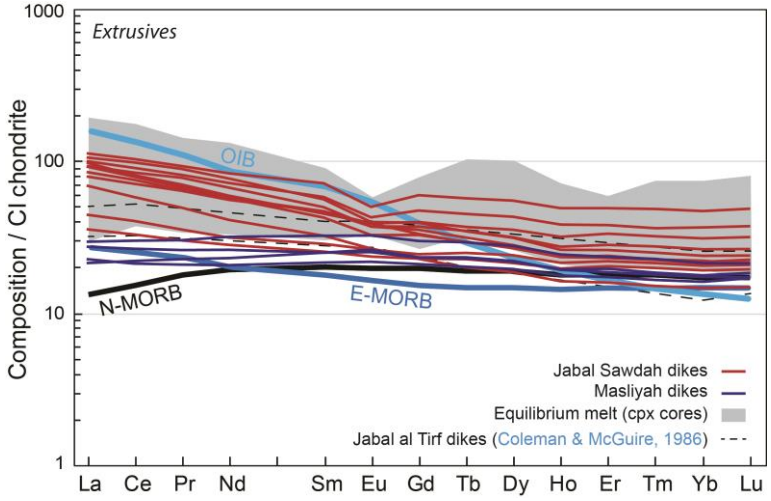


**Fig. 14.**